(FOR STANLEY DICKINSON)

REPORT DOCUMENTATION PAGE

AFRL-SR-BL-TR-00-

0639

1. AGENCY USE ONLY (*Leave Blank*)	2. REPORT DATE	3. REPORT TYPE AND DATES COVERED
	March 20, 2000	Final Report 7/1/94 - 6/30/98

4. TITLE AND SUBTITLE
AASERT-94 Analysis of Soviet DSS Records of Propagation and Modeling of Lg Blockage across Major Crustal Features

5. FUNDING NUMBERS
F49620-94-1-0408

6. AUTHORS
Smithson, Scott B. and James C. Schatzman

7. PERFORMING ORGANIZATION NAME(S) AND ADDRESS(ES)
University of Wyoming
P.O. Box 3355
Laramie, WY 82071-3355

8. PERFORMING ORGANIZATION REPORT NUMBER

9. SPONSORING / MONITORING AGENCY NAME(S) AND ADDRESS(ES)
AFOSR / NM
110 Duncan Avenue, Suite B115
Bolling AFB, DC 20332-8080

10. SPONSORING / MONITORING AGENCY REPORT NUMBER

11. SUPPLEMENTARY NOTES

12a. DISTRIBUTION / AVAILABILITY STATEMENT
no limitations

12b. DISTRIBUTION CODE

13. ABSTRACT *(Maximum 200 words)* Analysis of "Quartz" data resulted in two main conclusions directly relevant to the problem of nuclear test discrimination: 1) the uppermost mantle velocity and attenuation structure is significantly heterogeneous, and 2) the propagation of regional phases, including Lg is highly sensitive to this heterogeneity, and to the variations in crustal structure. The uppermost mantle is significantly heterogeneous, with vertical and horizontal velocity contrasts, high-and low-velocity zones, Moho topography, and two apparently regional reflecting boundaries present at 60-90 and 120-140 km depth. Such a complex structure would cause variations of amplitudes of Pn and Sn phases that cannot be accounted for by using traditional simplified 1-D models of the uppermost mantle. The Lg phase from PNE 323 is strong at distances below 500-700 km and at frequencies below 1.5-2.0 Hz, but is quickly attenuated with distance and nearly disappears between 1200-1400 km from the PNE. Thus in its amplitude-offset dependence, Lg propagation along the West Siberian Basin differs significantly from the propagation within the Baltic Shield where the absolute value of Lg amplitude appears to be substantially stronger, and no indications of its relative attenuation are found, even though the shot point is in a sedimentary basin. Compared to Lg, the S-wave from PNE 323 propagates effectively to regional ranges of about 2000 km, after which it becomes much weaker at teleseismic distances, although it still can be distinguished in the records. Important conclusions can be made from a comparison of Lg and S-wave amplitude. Lg quickly decreases in amplitude (faster than S-wave) during its propagation across the West Siberian Basin, whereas Lg from a PNE in a sedimentary basin effectively propagates in the Baltic Shield region. This observation suggests that the principal cause of the low amplitudes of short-period Lg form "Quartz" is the scattering or attenuation of Lg during its propagation within and below the sedimentary basins and not the source coupling. Eight graduate students were supported on the project.

14. SUBJECT TERMS

15. NUMBER OF PAGES

16. PRICE CODE

17. SECURITY CLASSIFICATION OF REPORT	18. SECURITY CLASSIFICATION OF THIS PAGE	19. SECURITY CLASSIFICATION OF ABSTRACT	20. LIMITATION OF ABSTRACT
Unclassified	Unclassified	unclassified	

NSN 7540-01-280-5500

Standard Form 298 (Rev. 2-89)
Prescribed by ANSI Std. Z39-1
298-102

Analysis of Soviet DSS Records for Propagation and Modeling of L_g Blockage across Major Crustal Features

EXECUTIVE SUMMARY

Students listed below have participated in this research project to calibrate discriminants for nuclear test monitoring. We have developed two-dimensional P-wave velocity models for the crust and for the upper mantle along the 3800-km-long Deep Seismic Sounding profile (DSS) "Quartz" from Kola across the Ural Mountains to the Altai Mountains in Russia sourced by 42 chemical explosions and 3 PNEs. Two-dimensional effects play a principal role in L_g propagation and its use as a seismic discriminant. To develop our model, we analyze the data obtained using 28 chemical explosions along the northwestern half of the profile. Applying a travel-time tomographic inversion method, we developed a velocity model and estimates of its resolution. Two important resolved features of the model are: 1) high velocity block at the base of the crust under the Baltic Shield, 2) crustal roots under the Ural Mountains. Using the data from 2 nuclear explosions in the same part of the profile we developed a 2-D upper mantle P-wave velocity model. The model supports the conclusion of the roots under the Urals, and suggests a southeast dipping low-velocity zone in the upper mantle. A high-frequency phase following teleseismic P_n from the PNEs is interpreted as a "whispering gallery" phase and is used to estimate attenuation within the upper mantle. L_g from 2 PNEs is blocked between sedimentary basins and the Ural Mountains. A marine-land profile recorded from the Barents Sea to the Kola Peninsula shows a crustal thickness of about 42 km at the coast. Data from continuing studies of the area by Russians will be available to us to better constrain the Barents-Kola transition. Methods for computer simulation of L_g propagation are developed using pseudospectral methods.

Students Supported:

Greg Baker, Graduate Student
Jeffrey Poet, Graduate Student
Laura Marston, Graduate Student
Katy Baxter, Graduate Student
Jennifer Adkins, Graduate Student
Ragnar Rasmussen, Graduate Student
Shawn Murphy, Graduate Student
Kevin Lielke, Graduate Student

Presentations:

Morozova, E. A., Morozov, I. B., Smithson, S. B., Schatzman, J. C., and Solodilov, L. N.; 1994, Studies of Pn, Sn and L_g wave propagation across major crustal structures using PNEs, in, Proc. Of the 16th PL/DARPA Seismic Research Symposium, Thornwood, Sept., 1994, PL-TR-94-2217, ADA284667.

Morozova, E. A., Morozov, I. B., and Smithson, S. B.; 1995, Evidence for upper mantle heterogeneities from the nuclear-shot sourced "Quartz" long seismic profile (abs.), Seis. Res. Lett., 66, n. 2, p. 40.

Schueller, W., Morozova, E. A., Morozov, I. B., and Smithson, S. B.; 1995, Tomographic inversion for two-dimensional crustal and upper mantle structure along the "Quartz" profile, Russia (abs.), Abstracts, IUGG XXI General Assemble, Boulder, p. A398.

Morozov, I. B., Schueller, W., Morozova, E. A., and Smithson, S. B.; 1995, Two-dimensional crustal and upper mantle velocity models from profile "Quartz" , Russia. Proceeding 17th Seismic Research Symposium on Monitoring a Comprehensive Test Ban Treaty, Sept., 1995, PL-TR-95-2108, p. 657-666.

Schatzman, J. C., and Meng, Z., 1995; A spectral scheme for viscoelastic seismic modeling, Proceedings of the 18th Annual Seismic Research Symposium on Monitoring a Comprehensive Test Ban Treaty, Sept., 1995, PL-TR-95-2108, p. 496-503.

Schueller, W., Morozov, I. B., and Smithson, S. B.; 1997, Crustal and uppermost mantle velocity structure of northern Eurasia along the profile "Quartz", Bull. Seis. Soc. Amer., 87: 414 - 426.

Morozov, I., Morozova, E., Ganchin, Y., and Smithson, S., 1996, L_g propogation across northern Eurasia recorded by profile "Quartz". Proceedings of the 19th Annual Seismic Symposium on Monitoring a Comprehensive Test Ban Treaty, Sept. 1996.

Morozova, E. A., Morozov, I. B., and Smithson, S. B., 1997, Heterogeneity of the uppermost Eurasian mantle along the DSS profile "Quartz", Russia; Fuchs (ed), Upper Mantle Heterogeneities from Active and Passive Seismology, pg. 139 - 146.

Morozov, I. B., Morozova, E. A., and Smithson, S. B., 1997, Observation of Lg and S-wave propagation along the ultra-long range profile "Quartz", Russia; Fuchs (ed), Upper Mantle Heterogeneities form Active and Passive Seismology, pg. 147 - 154.

Morozov, I. B., Morozova, E. A., Smithson, S. B., and Solodilov, L. N., 1998, 2-D image of seismic attenuation beneath the Deep Seismic Sounding Profile "Quartz", Russia, Pure Appl. Geophys., 153: 311 - 343.

Morozov, I. B., Morozova, E. A., Smithson, S. B., and Solodilov, L. N., 1998, On the nature of the teleseismic Pn phase observed on the Ultralong-Range Profile "Quartz", Russia, Bulletin of the Seismological society of America, 88: 62 - 73.

Table of Contents

Chapter 1

The teleseismic P_n in the ultra-long profile "Quartz", Russia

Elena Morozova, Igor Morozov and Scott Smithson

The long-range Russian profile "Quartz", studied in this report, consists of 42 chemical explosions and 3 PNEs. PNE records from the "Quartz" profile (Figure 1) show a consistent sequence of primary P-wave refractions in the first breaks observed to the maximum offset of 3145 km (Figure 2). Based on the analysis of the first arrivals, Mechie et al. (1993) derived 1-D velocity models for different PNEs, and Ryberg et al. (1996) proposed a 2-D model of the mantle velocity structure, using all three PNEs of the profile (Figure 1).

Due to high energy of the sources, PNE records are abundant in seismic phases as secondary arrivals (Figure 2). Reflections from the 410 km and 660 km discontinuities in the mantle and a number of multiples are easily recognized (Figure 2). Our attention will be concentrated on the phase which is not obvious in the unfiltered gathers, but becomes dominant after a high-pass filtering of the records above approximately 5 Hz (Figure 3).

Such high-frequency teleseismic P_n phases, and corresponding S_n phases propagating within the uppermost mantle to 2000-3000 km distances were observed by many authors (e.g., Molnar and Oliver, 1969; Heustis et al., 1973; Walker 1997). These phases efficiently propagate through continental shields and deep-ocean basins, but appear to be blocked by major suture zones (Molnar and Oliver, 1969). Although these phases are generally accepted as due to some sort of waveguide mechanism, no agreement about the details of this mechanism exists. Depending on the mantle structure beneath the Moho, several models of these high-frequency teleseismic phases have been proposed: whispering-gallery waves within the upper mantle (Stephens and Isacks, 1977; Menke and Richards, 1980), guided wave in a high-velocity layer above a low-velocity layer (Mantovani et al., 1977), or transmission through a low-velocity layer beneath the Moho (Sutton and Walker, 1972). Long incoherent codas of P_n and S_n arrivals are explained by scattering of high-frequency waves within the crust and upper mantle (Richards and Menke, 1983; Menke and Chen, 1984) together with reverberations in the water column (Sereno and Orcutt, 1985, 1987).

Ryberg et al. (1995), who first observed this band of incoherent high-frequency energy in "Quartz" records, proposed a model of a scattering waveguide located immediately below the Moho. Using simulations with the reflectivity method (Fuchs

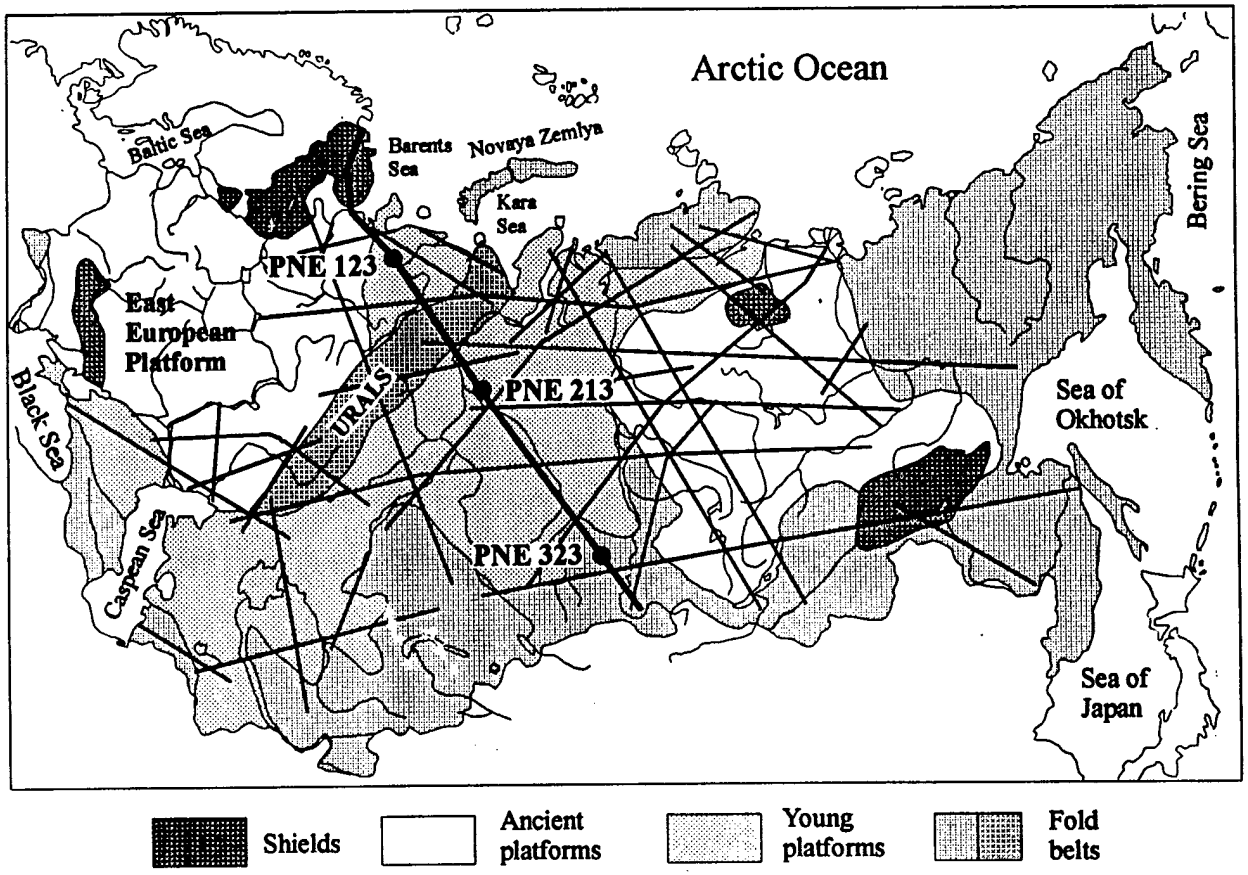

Figure 1. Map of the former USSR showing major DSS profiles using nuclear explosions. "Quartz" is shown in bold line; circles indicate the locations of three nuclear explosions recorded by the profile. The data from the southern PNE (shot point 323) are used in this paper.

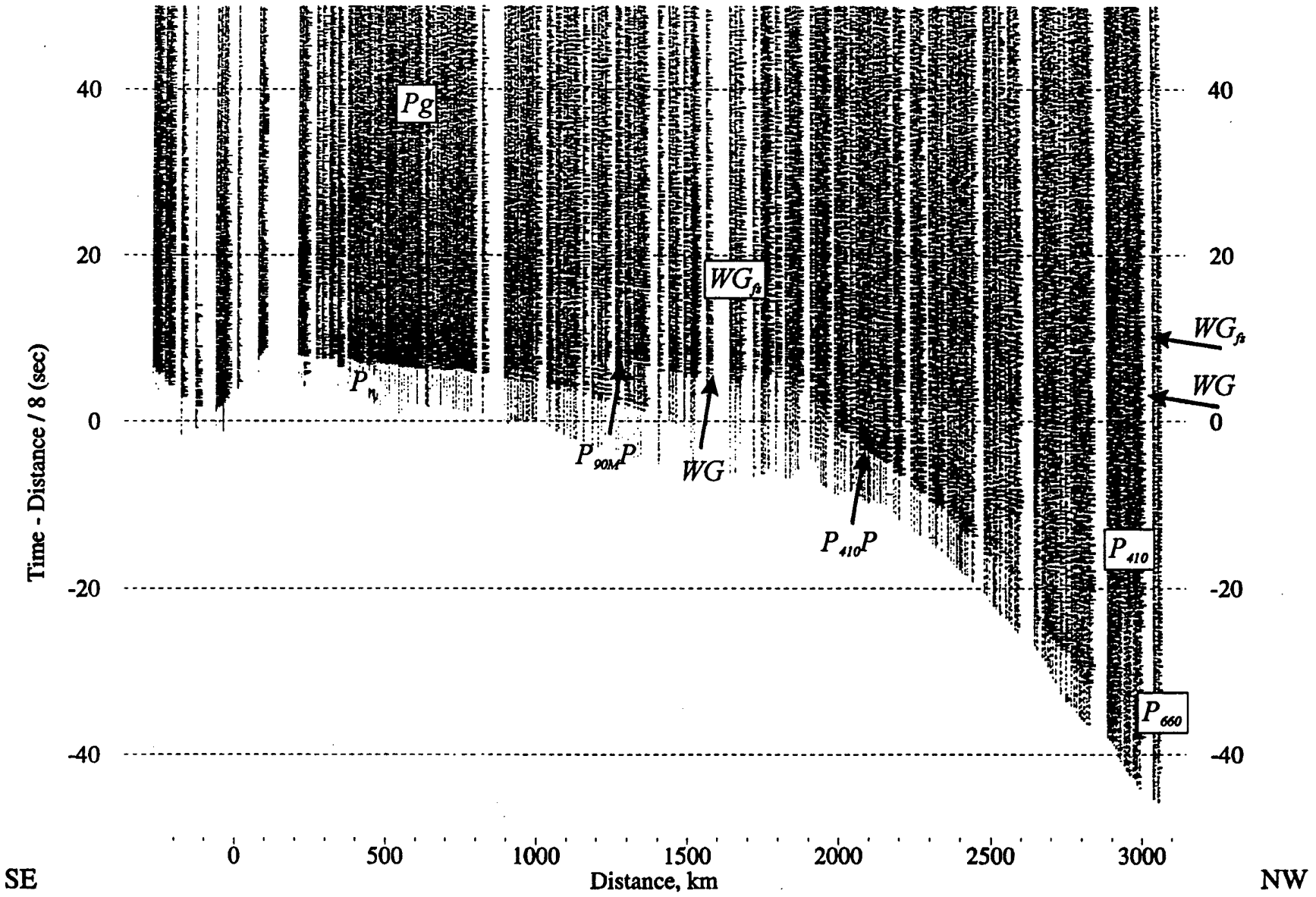

Figure 2. Vertical component record section from the southern PNE of profile "Quartz". This nuclear shot is characterized by the highest amplitude of high frequency signal. Reduction velocity is 8 km/sec. P_n and the first whispering-gallery mode (WG) discussed in this paper are indicated.

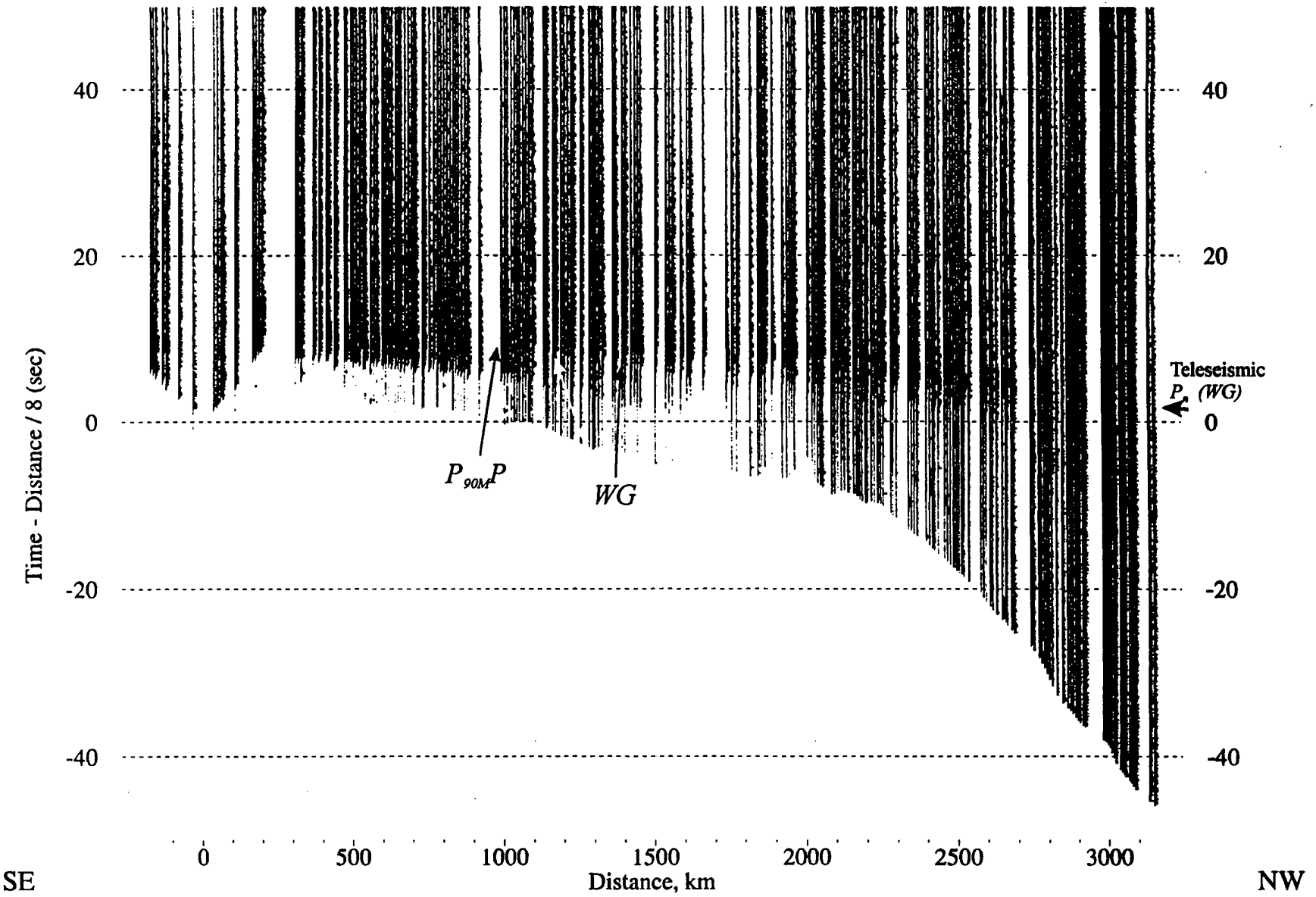

Figure 3. 3-component instantaneous vector amplitude gather of high-pass filtered records from the southern PNE (Morozov and Smithson, 1996). Vector amplitude provides a more stable amplitude pattern facilitating identification of the WG mode at smaller offsets. Reduction velocity is 8 km/sec, corner frequency of the filter 5 Hz. This record is dominated by incoherent energy propagating with an apparent velocity of about 8.1 km/sec, corresponding to the teleseismic P_n phase. We associate this phase with two low-order WG modes.

and Müller, 1971), Tittgemeyer et al., (1996) demonstrated that a high-frequency phase with an apparent velocity of about 8.1 km/sec can propagate by means of a multiple scattering through a 80-km thick random sequence of thin layers below the Moho.

Although presenting a possible propagation mechanism, the model by Ryberg et al. (1995) and Tittgemeyer et al. (1996) does not account for two important details in the kinematics of this high-frequency phase—the increase in its apparent velocity within the offset range of 1000-1700 km, and the presence of a high-frequency and a high-velocity event at offsets exceeding 2500 km (Figure 3). Also, it does not explain the relation of the teleseismic P_n to other low-frequency phases, in particular, the coincidence of the onset of this phase in the offset range 1000-1700 km with the "internal multiple" m indicated earlier by Mechie et al. (1993) (Figure 2).

TELESEISMIC P_n IN "QUARTZ" RECORDS

Analyzing the nature of the high-frequency teleseismic P_n phase in "Quartz" records, we need to explain three major observed characteristics of this phase:

1) its travel-time dependence and relations to other seismic phases;
2) clear separation in frequency content from the lower-frequency deep refractions;
3) the absence of a sharp onset and a long incoherent coda.

Travel-time analysis

The key observation distinguishing our interpretation from that by Ryberg et al. (1995) is the shape of the travel-time curve for the onset of the high-frequency energy at smaller offsets at which it is observed (1100-1600 km; Figure 3). The overall shape of the travel-time curve of these onsets can be confidently established as following a pattern of a multiple reflection rather than as being a continuation of the P_n phase (Figure 3). To examine the travel-time pattern of seismic phases found in the records, we employ 2-D ray tracing in a spherically-symmetric 1-D model. With the degree of accuracy at which the picking of the onset of the teleseismic P_n can be performed, a 1-D model developed using the first breaks picked from the records of the same southern PNE is quite appropriate (Figure 4A). The velocity column associated with this PNE is characterized by a strong velocity gradient between 90 and 120 km, a narrow low-velocity zone (LVZ) between 140 and 155 km, and a prominent LVZ with a low velocity gradient between 195 and 380 km depth. This velocity structure explains the first breaks very well, including the 400-km long shadow zone between the offsets from 1500 to 1900 km (Figure 2; see also Mechie et al. 1993). Ray tracing through this velocity structure leads us to interpret the high-frequency teleseismic P_n as a "whispering-gallery" phase (Figure 4B).

The results of travel time modeling of the main phases propagating in this 1-D velocity strucure summarized in (Figure 5D) and compared to the high-frequency record section in Figure 6 show that the first whispering-gallery mode corresponds to

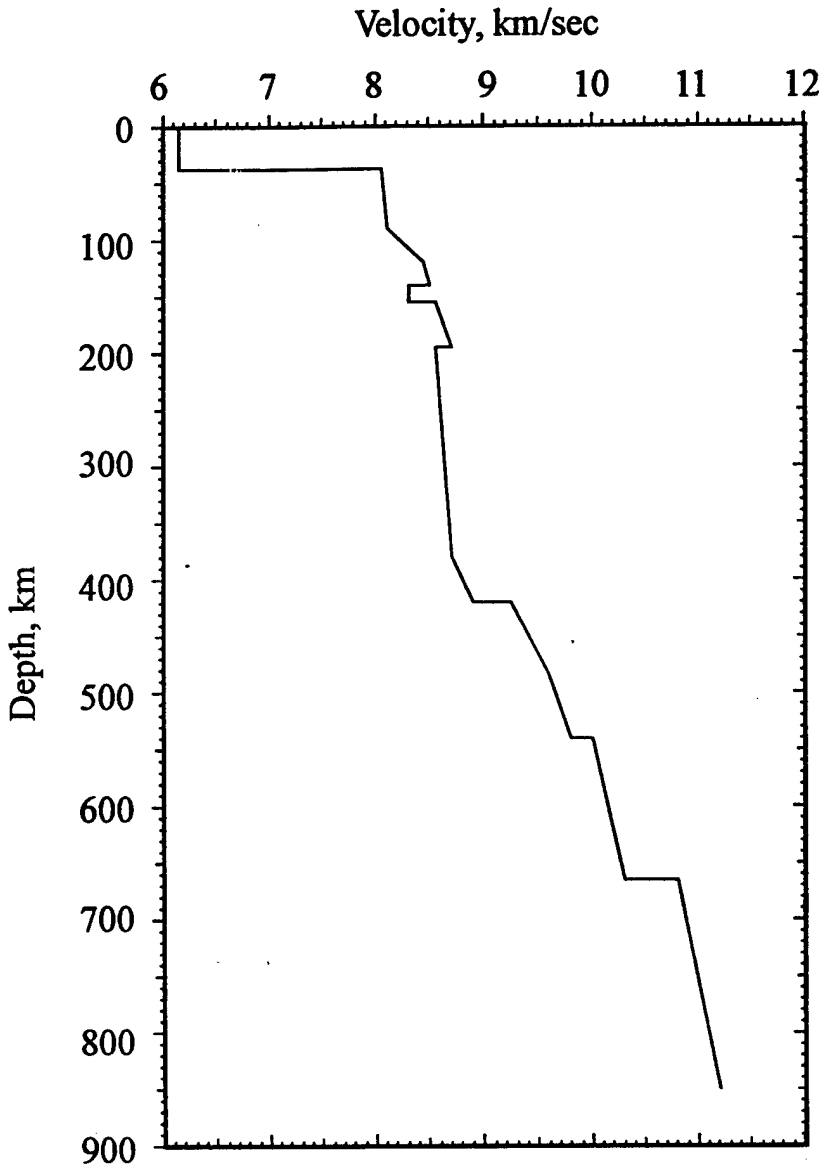

Figure 4A. 1-D velocity model obtained using the first breaks of the southern PNE by Mechie et al. (1993). We used this model for 2-D ray tracing in our analysis of the kinematics of the teleseismic P_n. Note LVZ at 140-155 km depth and the prominent LVZ below 195 km.

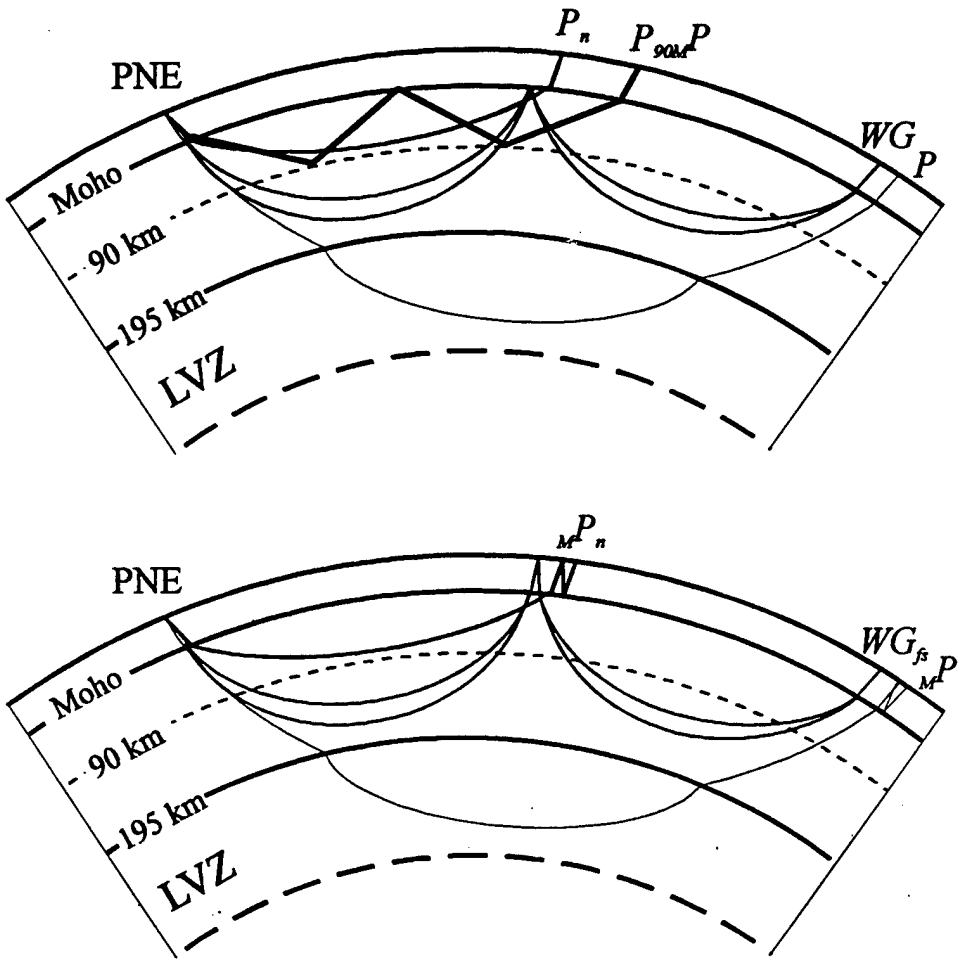

Figure 4B. A summary of our interpretation of observed high-frequency phases in "Quartz" records. Not drawn to scale.

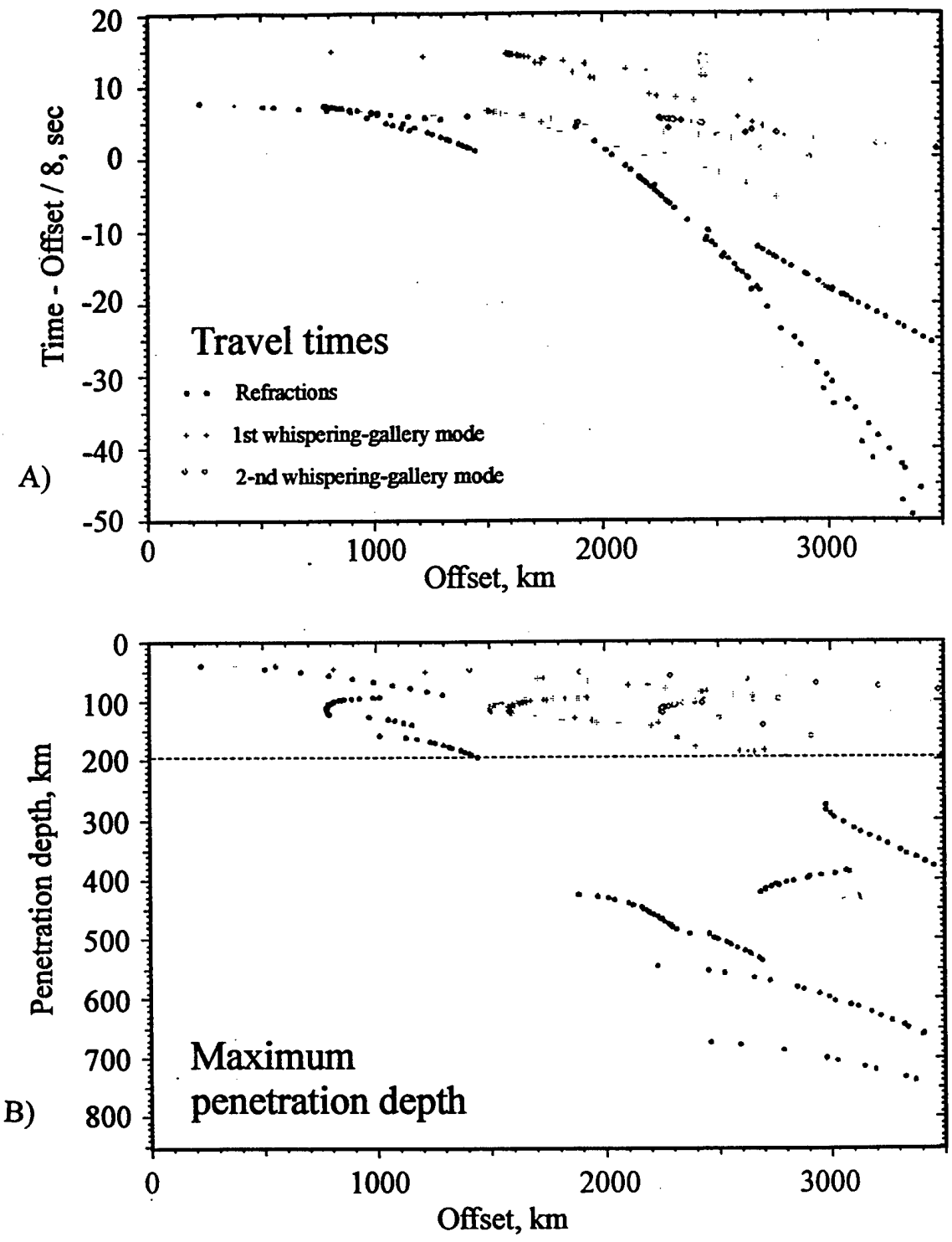

Figure 5. *A)*: The results of ray tracing in the velocity model of Figure 4A. A) travel time curves of the major phases. *B)*: maximum penetration depths of refracted waves. *C)*: travel times below the level of 195 km. Note that the far-offset refracted phases travel within the LVZ for about 60-70% of their total propagation times below this depth *D)*: a sketch of the major seismic phases , reserved in Quartz records (Figure 2): P_n, P, P_{410}, P_{660}, primary refractions; WG_1, WG_2 - whispering-gallery modes; WG_{fs} - free-surface whispering-gallery mode; $P_{195}P$,$P_{410}P$ - reflections; P_{90M} - a multiple between 90 km and Moho. Gray circles indicate the triplication points of WG modes.

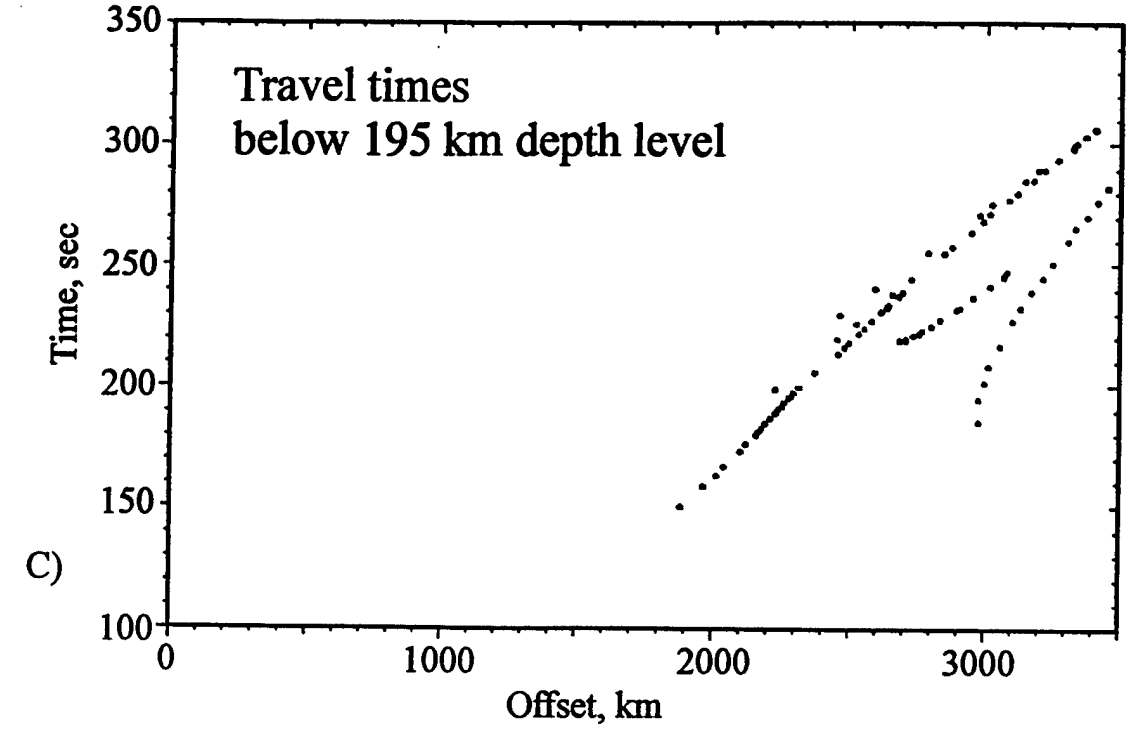

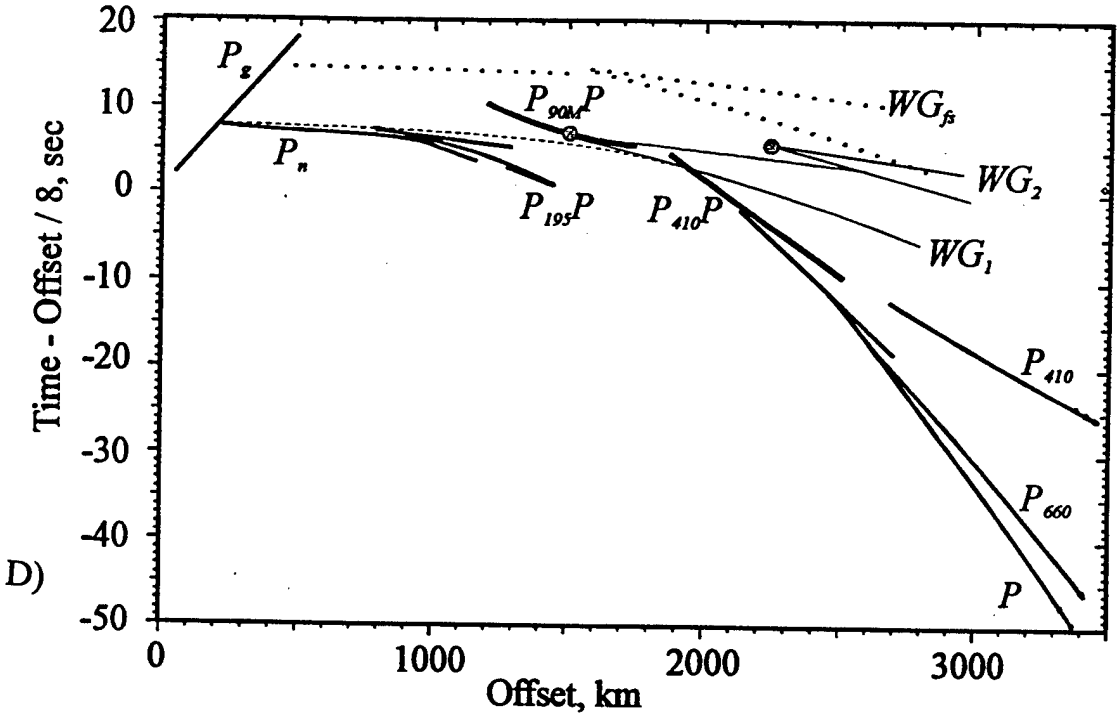

Figure 5. Continued

the observed teleseismic P_n throughout its entire observation length. The whispering-gallery mode appears at offsets of about 400-500 km and has a significant amplitude in between offsets of 1500 to 2000 km, representing the first strong arrival in this region. Toward smaller offsets, its travel-time curve can be continued as that of a multiple between a reflector at about 90 km depth and the Moho labeled in Figure 2. At larger offsets, this phase continues to the end of the offset range with an apparent group velocity of 8.2 km/sec (Figure 5). Note that the second whispering-gallery mode appearing at the offsets of about 2200 km can be also identified in the records (compare Figure 4A to Figure 6). Due to variations of the velocity gradient above 140 km depth), this whispering-gallery mode exhibits a triplication at about 1800-2000 km, with the fast branch having an apparent velocity of 8.8 km/sec (Figure 5).

Based on the above observations—on high amplitude of the whispering-gallery phase observed from 1500 to 2000 km of offset in unfiltered records, on the travel-time match of this phase with the teleseismic P_n throughout the entire offset range, and on the observation of the triplication of the teleseismic P_n at about 2000 km—we conclude that the whispering gallery mode presents a good explanation of the kinematics of the observed high-frequency teleseismic P_n phase. As we see in Figure 6, the travel-time curve of the teleseismic P_n *does not* approach that of the ordinary P_n with decreasing offset, but follows the moveout of a multiple reflection from a depth of approximately of 90 km. Therefore, the teleseismic P_n cannot originate immediately below the Moho, as it was suggested by Ryberg et al., (1995) and Tittgemeyer et al. (1996), but should effectively be produced by the strong velocity gradient between 90 and 120 km depth (Figure 4A).

To estimate frequency content of various arrivals, we normalize the traces using their total RMS values and calculate the power spectrum of the recorded signal in every trace within 15-30-sec time windows including the first arrivals and the teleseismic P_n, and also in a 20-40 sec "noise window" beginning 100 sec after the onset of teleseismic P_n (Figure 9.). The low-frequency component dominates both first arrival and the teleseismic P_n, and its amplitude is approximately the same in both these time windows. At the frequencies between 4 and 6 Hz, however, the power spectral density in the first arrivals is lower by 10-12 dB than in the teleseismic P_n (Figure 9.). At the same time, Figure 9. shows that this peak of high-frequency teleseismic P_n exceeds the source-generated noise 100 sec after its onset by only about 10-15 dB.

The 10-12 dB difference in the spectral power of the teleseismic P_n and of the deeper refractions accounts for the dominance of the teleseismic P_n phase in the high-pass filtered records (Figure 3). This means that the far-offset refracted waves are subject to higher effective attenuation during their propagation. As we show in the following section, propagation paths of these far-offset refacted waves differ substantially from those of the waveguide modes, and thus this relative energy loss in the high-frequency component can be naturally associated with depth-dependence of seismic attenuation within the mantle.

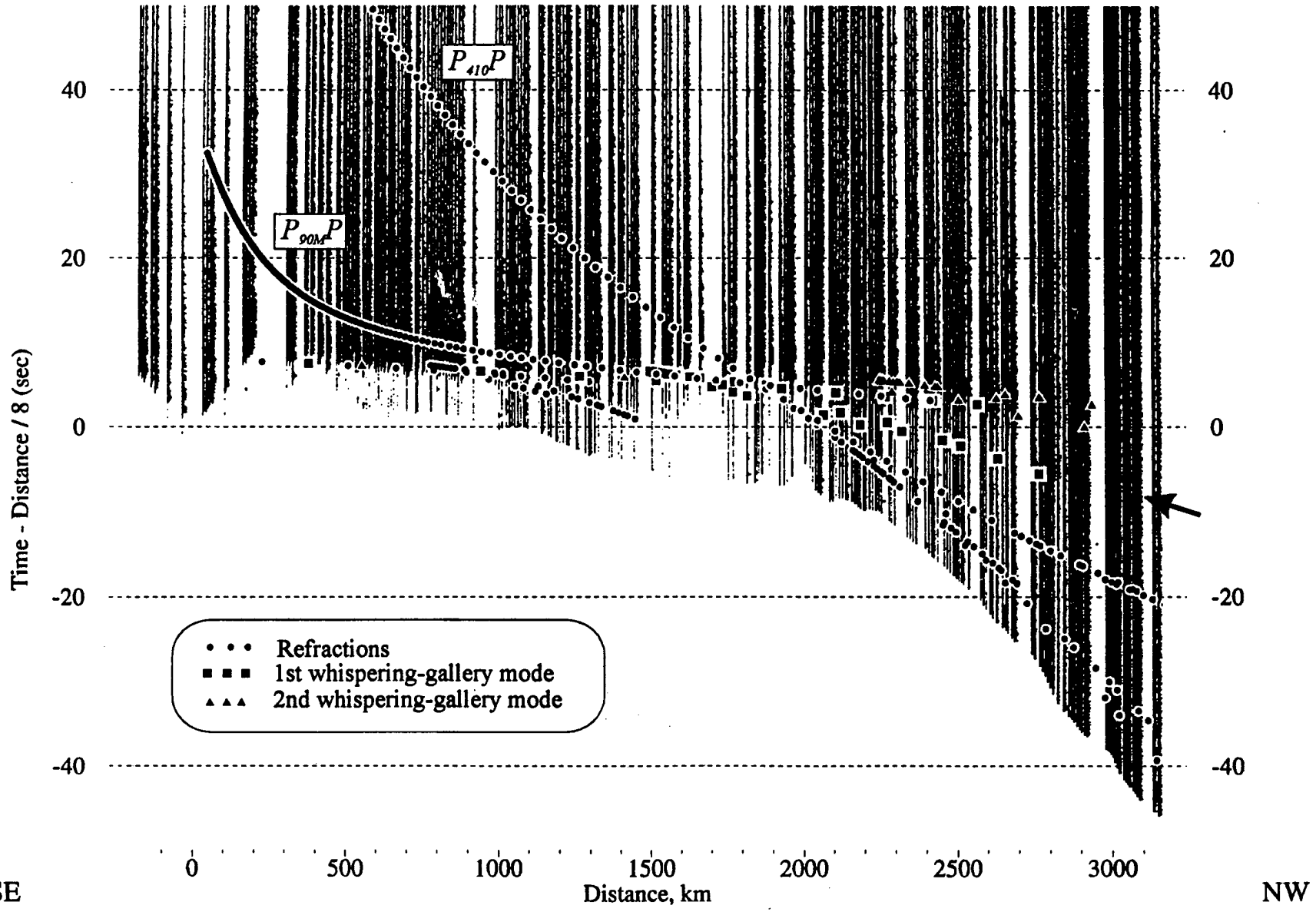

Figure 6. The same travel-time points as in Figure 5 overlain over the high-pass filtered record shown in (Figure 4A). . The whispering-gallery modes correspond to the onset of the high-frequency teleseismic P_n. A triplication of the whispering-gallery mode is observed, but can be followed to farther distances than in the modeled travel-time curves (indicated by arrow). Travel-time curves of the reflection from the 410-km discontinuity and of the multiple between the Moho and 90-km depth are also shown.

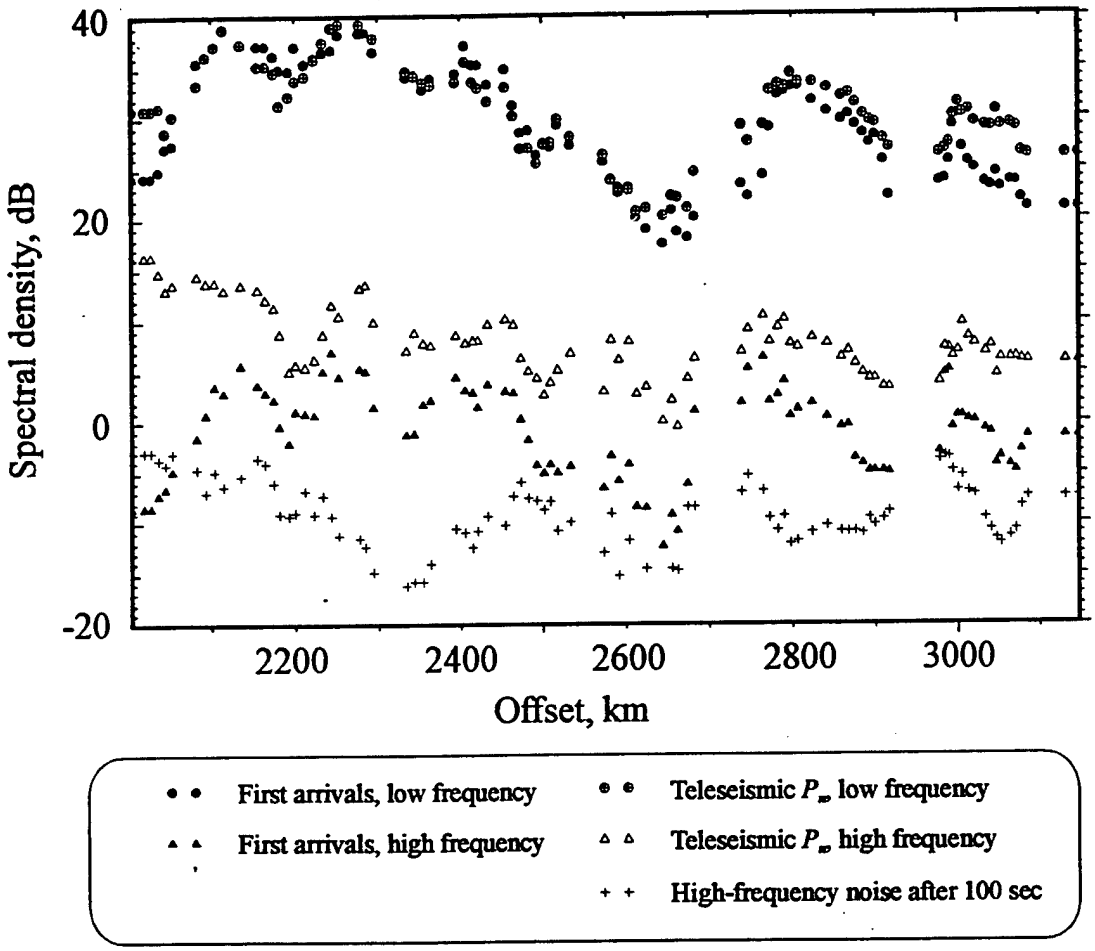

Figure 7. Ratios of the averaged power spectra within 0.5-2 Hz and 4-6 Hz in the offset range 2200-3000 km: a) first break window; b) teleseismic P_n window; c) high-frequency "post-shot noise", estimated at a signal level 100 sec after the onset of the teleseismic P_n. Note that the high-frequency teleseismic Pn exceeds the corresponding level in the first arrivals by about 8-12 dB, but is above the post-shot noise by only 10-15 dB.

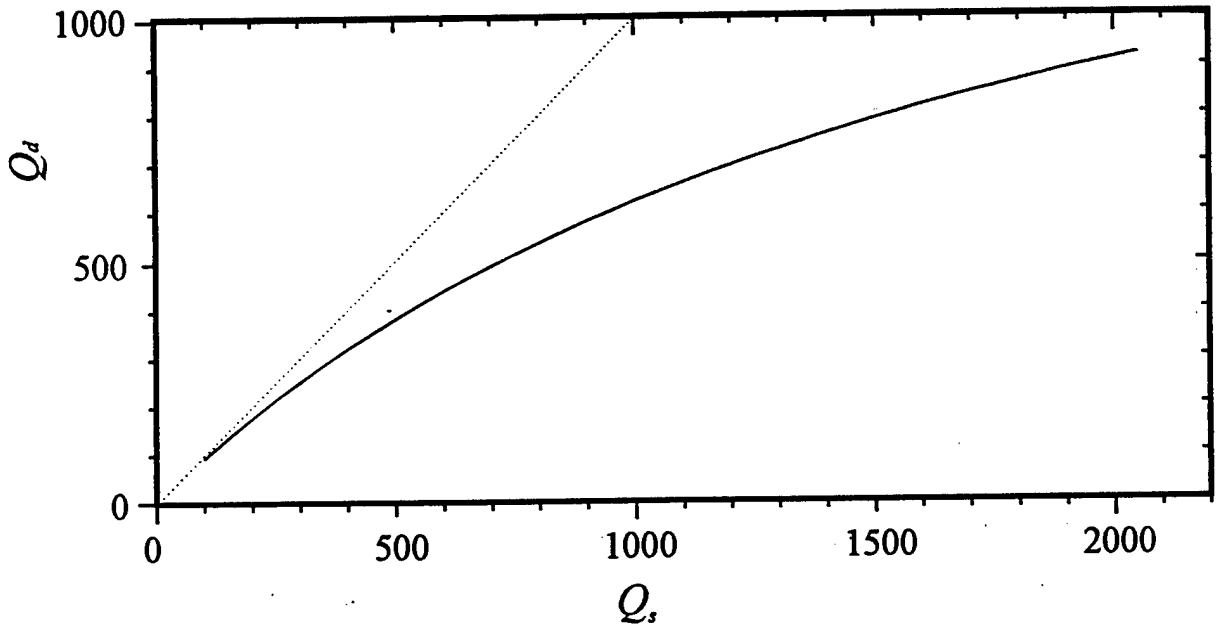

Figure 8. Constraint on the attenuation contrast at the top of the LVZ obtained from the ratios of power spectra of deep refractions and of the teleseismic P_n using Equation (2). The quality factors Q_s (above the 195 km level) and Q_d (below this level) must correspond to a point below the graph. Dotted line represents the relation Q_d=Q_s, highlighting the contrast between Q_d and Q_s increasing with Q_s.

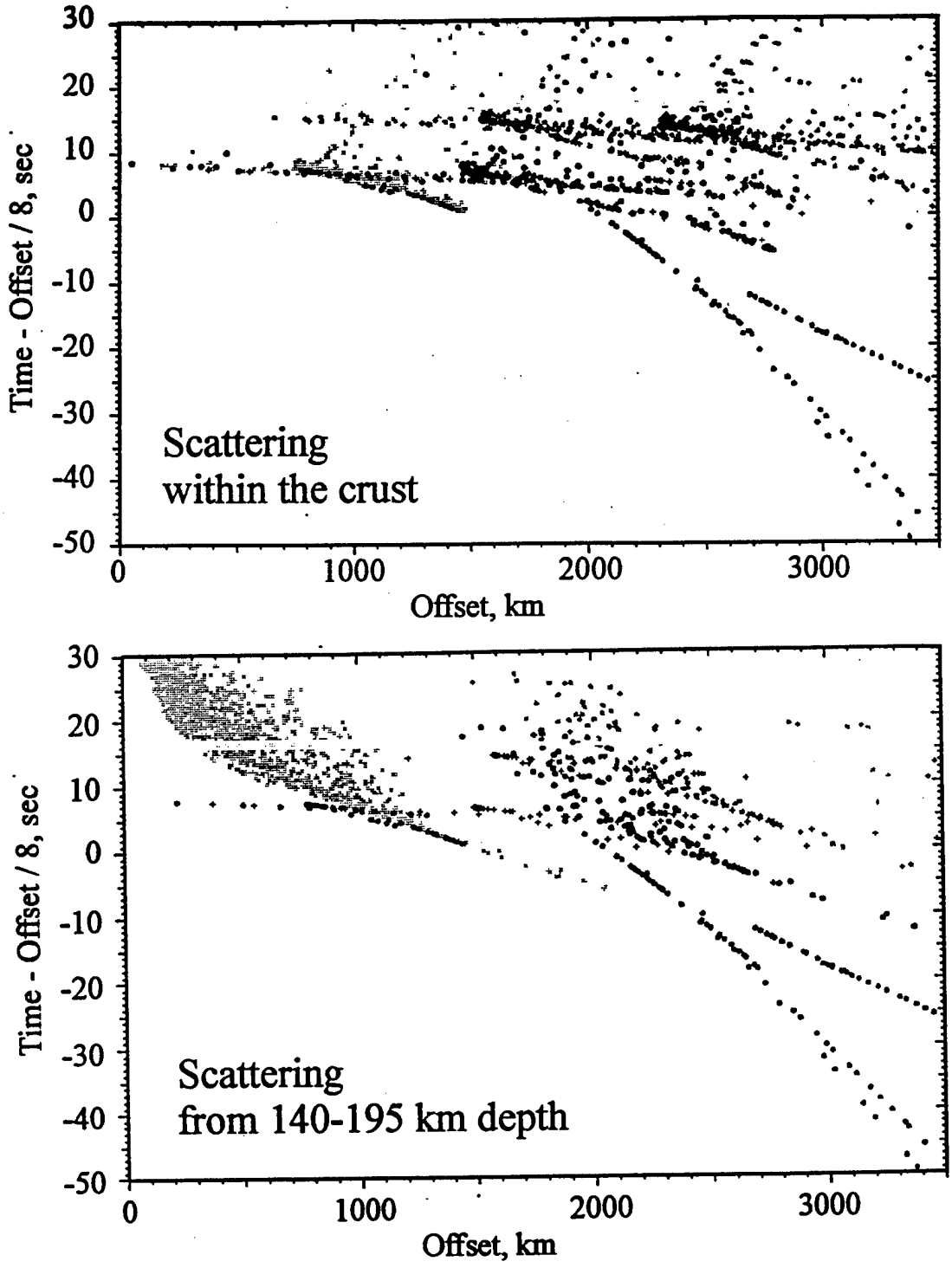

Figure 9. Travel-time plots obtained using ray tracing in 1-D velocity model with random scatterers located within two depth ranges. *Top:* first-order scattering within the depth range 0-140 km; *bottom: :* 1 first-order scattering within the depth range 140-195 km. Free-surface and Moho multiples are included in all cases. The rays are not allowed to penetrate into the LVZ (deeper then 195 km). Black dots represent the scattering of direct refracted waves and of WG mode, gray dots show the scattering of the free-surface WG mode and Moho multiples.

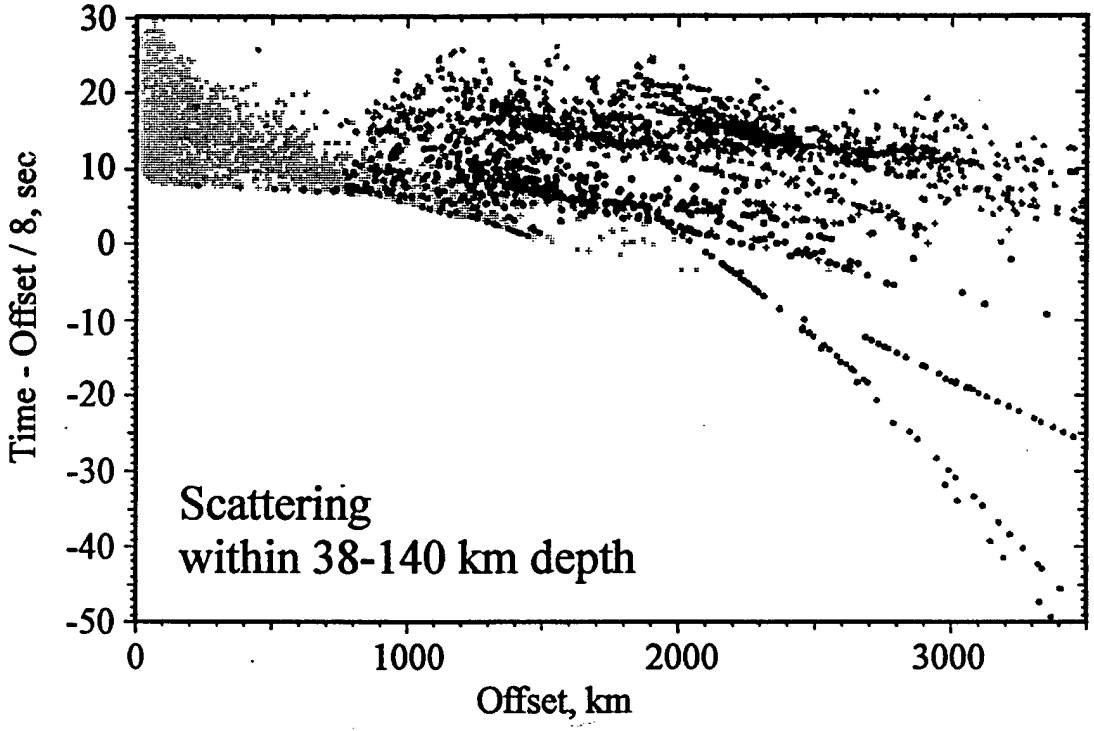

Figure 9. Continued.

High frequency of the teleseismic P_n

A simple "first-order" explanation of the differences in frequency content of the seismic phases shown in (Figure 4B) is readily obtained by an examination of the penetration depth diagram shown in Figure 5B. The near-offset high-frequency refracted mantle wave seen up to nearly 1500 km offset and the high-frequency, whispering- gallery modes observed between the offsets of 800 km and 2800 km do not dive deeper than 195 km into the mantle (195 km is the depth of the top of the prominent lower LVZ in the model by Mechie et al. (1993)—see Figure 4A). On the contrary, all far-offset refractions penetrate at least to the level of 270 km. This observation suggests that the low-velocity structure below the level of 195 km may cause significant attenuation of the frequencies near and above 5 Hz. Since the total propagation times of the deep phases are *smaller* than those of the waveguide modes, a comparatively sharp increase in the attenuation should occur near the 195-km level.

To constrain the amounts of this attenuation, we calculate the relative energy dissipation factor between the two frequencies during the propagation of a deep refracted wave:

$$A_{12}^{deep} = 10 \cdot \lg\left(\frac{E(f_1)}{E(f_2)}\right) = 10 \cdot \lg e \cdot \left(\frac{2\pi}{Q_s} t_s + \frac{2\pi}{Q_d} t_d\right)(f_2 - f_1), \qquad (1)$$

describing the increase in the ratio of the low-frequency spectral density (frequency f_1) to the high-frequency spectral density (frequency f_2), in dB. In this equation, we disregard geometric spreading, and consider a simple two-layer model of the mantle attenuation, with the quality factors Q_S in the "shallow" part above the level of 195 km, and Q_d below this level ("deep" part). The times the deep refracted wave travels within these layers are denoted as t_S and t_d, respectively. Subtracting from the quantity defined in Equation (1) a similar ratio for the whispering gallery arrival, we obtain an expression for the observed logarithmic relative contrast between the 5 Hz and 1.5 Hz spectral constituents of these phases:

$$A_{12}^{deep} - A_{12}^{waveguide} = 10 \cdot \lg e \cdot \left(\frac{2\pi}{Q_s} t_s + \frac{2\pi}{Q_d} t_d - \frac{2\pi}{Q_s} t_{wg}\right)(f_2 - f_1), \qquad (2)$$

where t_{wg} is the total travel time of the whispering gallery mode, taken at the same offset.

Assuming that the spectral power ratio in the Equation (2) corresponds to the observed 10-12 dB change in spectral ratios (Figure 9.), we obtain a constraint on the values of quality factors Q_S and Q_d above and below the 195-km level shown in Figure 8. Although this estimate does not constrain the attenuation in the uppermost mantle, it demonstrates that an increase in attenuation below the 195 km level is necessary to explain the observed difference in the high-frequency content between the more shallow and deep refractions and reflections (Figure 8). Assuming that the attenuation above the LVZ corresponds to $Q_s \approx 1200$, we obtain from Equation (2) the value $Q_d \approx 700$ for the quality

factor below the 195-km level (Figure 8). Note that the contrast between the attenuation above and within the LVZ increases with increasing Q_s.

Multiples and scattering

The above travel-time simulations correctly indicate the position of the onset of the teleseismic P_n but do not explain the absence of a sharp onset of this phase, which is marked by and the presence of a long, incoherent coda, Figure 6 shows that modeled travel time curves of the whispering-gallery (WG) modes terminate near offsets of 2500-2800 km, whereas the phase can be traced further on the seismograms. All these features can be explained by scattering occurring within the crust and upper mantle.

Three prominent reflectors—the free surface, the Moho, and the top of the basement—create long trains of multiples in the records. Three free-surface/Moho multiples of P_n and at least two multiples of the first WG phase are present. At higher frequencies, these multiples become more abundant and are complemented by random scattering from crustal and upper mantle structures. On the scale of our study, this scattering creates an incoherent pattern of source-generated noise slowly decaying within the characteristic times corresponding to 1-3 passes of the seismic waves through the crust (10-30 sec).

In our modeling, we will be concerned only with the kinematics of the scattering by introducing random scattering points into all rays shown in (Figure 4B). The scatterer depths and angles are uniformly distributed. Thus the pattern of modeled offset-traveltime pairs represents a pattern of probable scattering paths from point scatterers. To produce a more physically realistic picture of scattering including scattering amplitudes, a more rigorous modeling using a 2-D mantle velocity/attenuation model is certainly desirable.

The results of ray tracing in the same 1-D velocity model) with random scattering heterogeneities located within two depth ranges are shown in Figure 9. We modeled the kinematics of the first-order scattering occurring within the crust (0-38 km depth), above the first LVZ (38-140 km depth), and below this LVZ to the top of the second velocity inversion (140-195 km depth). In all cases, we included the first multiples from the free surface and from the Moho boundary. Figure 9 shows that these first-order scattering effects complemented by multiples account for the about-20-sec long codas of the WG modes. The scattering within the crust also creates long P_g-like tails of scattering lasting for about 40-50 sec in our simulation. Since up to 3-4 crustal multiples are actually observed in the PNE records (Figure 2), we expect that the real scattering pattern involving 3-4 scattering and free-surface/Moho/basement reflection events would be much more complicated and extended in time.

A significant feature of the high-frequency wavefield is the presence of energy propagating faster than the teleseismic Pn at offsets exceeding 2700 km (Figure 3); also marked with an arrow in Figure 6. The fast branch of WG mode terminates at offsets of about 2700 km due to its plunging into the LVZ (Figure 5). The deep scattering pattern

shown in the bottom of (1), however, shows that the scattering from the lid of LVZ tends to extend the fast WG mode to larger offsets. This observation suggests that the scattering increases immediately above the LVZ, probably in the form of low-angle scattering enhancing the far-offset part of WG mode.

The above observation of an increased scattering from the top of LVZ may have two important consequences. First, predominantly low-angle scattering may be an evidence of layering at or immediately above the top of LVZ. Second, the 40-50% increase in the attenuation within the LVZ might be due to the same scattering mechanism that manifests itself through the high-frequency energy recorded at the surface.

Coda

The high-pass filtered records show a long coda following the teleseismic P_n arrival (Figure 3). Amplitude decay does not show any coda that can be specifically associated with the region where the teleseismic P_n originates. Instead, we see a typical continuous energy dissipation probably due to multiple scattering within the crust. Also, as the above analysis (and an examination of the low-frequency records in Figure 2) shows, the coda of the whispering gallery mode is structured, representing a sequence of prominent Moho multiples and higher-order whispering gallery modes overlain by a complicated scattering pattern.

CONCLUSIONS

Based on our analysis of the secondary phases observed in the records from the ultra-long DSS profile "Quartz", we propose an interpretation of a high-frequency teleseismic P_n phase as a whispering gallery wave traveling within the gradient layer in the mantle below the Moho. This conclusion is supported by the travel-time forward modeling of all observed phases using a detailed 1-D velocity model derived earlier. The long incoherent coda of this phase is associated with the scattering of seismic waves within the crust and upper mantle and multiple reverberations within the crust, including its basement and the sedimentary cover. To explain the contrast in the frequency contents between the teleseismic P_n and other refracted and reflected phases recorded at offsets exceeding 1200 km, we infer an increase in attenuation within the prominent low-velocity zone beginning at the depth of 195 km. Above this level, the attenuation is not significant, and the scattering is moderate.

REFERENCES

Egorkin, A. V. and A. V. Mikhaltsev (1990). The Results of Seismic Investigations along Geotraverses, in *Super-Deep Continental Drilling and Deep Geophysical Sounding*, K. Fuchs, Y. A. Kozlovsky, A. I. Krivtsov and M. D. Zoback (Editors), Super-Deep Continental Drilling and Deep Geophysical Sounding, Springer, Berlin, 111-119.

Egorkin, A. V., and N. I. Pavlenkova, Studies of mantle structure in the U.S.S.R. territory on long-range seismic profiles, *Phys. Earth Planet Inter.*, *25*, 12-26, 1981.

Fuchs, K., and G. Müller, Computation of synthetic seismograms with the reflectivity method and comparison with observations, *J. R. Astronom. Soc.*, *23*, 417-433, 1971.

Heustis, S., P. Molnar, and J. Oliver, Regional S_n velocities and shear velocity in the upper mantle, *Bull. Seismol. Soc. Am.*, *63*, 469-475, 1973.

Kennett, B. Distance dependence of regional seismic discriminants, ??, 1993.

Kozlovsky, Y. A., The USSR Integrated Program of Continental Crust Investigations and Studies of the Earth's Deep Structure under the Globus Project, in *Super-Deep Continental Drilling and Deep Geophysical Sounding* Fuchs K., Kozlovsky Y. A., Krivtsov A. I. and Zoback M. D. (Editors), Springer, Berlin, 90-103, 1990

Mantovani E., F. Schwab, H. Liao, and L. Knopoff, Teleseismic S_n: A guided wave in the mantle, *Geophys. J. R. Astron. Soc.*, *51*, 709-726, 1977.

Mechie, J., A. V. Egorkin, K. Fuchs, T. Ryberg, L. Solodilov, and F. Wenzel, P-wave velocity structure beneath northern Eurasia from long-range recordings along the profile Quartz, *Phys. Earth Planet* Inter., 79, 269-286, 1993.

Menke, W. H., and P. G. Richards, Crust-mantle whispering gallery phases: A deterministic model of teleseismic Pn wave propagation, *J. Geophys.* Res., *85*, 5416-5422, 1980.

Molnar, P., and J. Oliver, Lateral variations of attenuation in the upper mantle and discontinuities in the lithosphere, *J. Geophys.* Res., *74*, 2648-2682, 1969.

Morozov, I. B., and Smithson, S. B., Instantaneous polarization attributes and directional filtering, *Geophysics*, 61, 872-881, 1996.

Ryaboy, V., Upper mantle structure studies by explosion seismology in the USSR, Delphic Associates, 1989, 138 pp.

Ryberg, T., K. Fuchs, A. V. Egorkin, and L. Solodilov, Observations of high-frequency teleseismic P_n on the long-range Quartz profile across northern Eurasia, *J. Geophys. Res.*, *100*, 18151-18163, 1995.

Ryberg, T., Wenzel, F., Mechie, J., Egorkin, A., Fuchs, K., and Solodilov, L., Two-dimensional velocity structure beneath Northern Eurasia derived from the super long-range seismic profile Quartz, *Bull. Seismol. Soc. Am.*, *86*, 857-867, 1996.

Schueller, W., I. B. Morozov, and S. B. Smithson, Crustal and uppermost mantle velocity structure of northern Eurasia along the profile Quartz, *Bull. Seismol. Soc. Am., in press*, 1997.

Sereno, T. J., and J. A. Orcutt, Synthesis of realistic oceanic P_n wave trains, *J. Geophys. Res.*, *90*, 12755-12776, 1985.

Sereno, T. J., and J. A. Orcutt, Synthetic P_n and S_n phases and the frequency dependence of Q of oceanic lithosphere, *J. Geophys. Res., 92*, 3541-3566, 1987.

Stephens, C., and B. L. Isacks, Toward an understanding of S_n: Normal modes of Love waves in an oceanic structure, *Bull. Seismol. Soc. Am., 67*, 69-78, 1977.

Sutton, G. H., and D. A. Walker, Oceanic mantle phases recorded on seismograms in the northwestern Pacific at distances between 7° and 40°, *Bull. Seismol. Soc. Am., 62*, 631-655, 1972.

Tittgemeyer, M., F. Wenzel, K. Fuchs, and T. Ryberg, Wave propagation in a multiple-scattering upper mantle—observations and modeling, *Geophys. J. Int., 127*, 492-502, 1996.

Walker, D. A., High-frequency P_n and S_n phases recorded in the western Pacific, *J. Geophys. Res., 82*, 3350-3360, 1977.

Figure Captions

Figure 1. Map of the former USSR showing major DSS profiles using nuclear explosions. "Quartz" is shown in bold line; circles indicate the locations of three nuclear explosions recorded by the profile. The data from the southern PNE (shot point 323) are used in this report.

Figure 2. Vertical component record section from the southern PNE of profile "Quartz". This nuclear shot is characterized by the highest amplitude of high frequency signal. Reduction velocity is 8 km/sec. P_n and the first whispering-gallery mode (WG) discussed in this report are indicated.

Figure 3. 3-component instantaneous vector amplitude gather of high-pass filtered records from the southern PNE (Morozov and Smithson, 1996). Vector amplitude provides a more stable amplitude pattern facilitating identification of the WG mode at smaller offsets. Reduction velocity is 8 km/sec, corner frequency of the filter 5 Hz. This record is dominated by incoherent energy propagating with an apparent velocity of about 8.1 km/sec, corresponding to the teleseismic P_n phase. We associate this phase with two low-order WG modes.

Figure 4A. 1-D velocity model obtained using the first breaks of the southern PNE by Mechie et al. (1993). We used this model for 2-D ray tracing in our analysis of the kinematics of the teleseismic P_n. Note LVZ at 140-155 km depth and the prominent LVZ below 195 km.

Figure 4B. A summary of our interpretation of observed high-frequency phases in "Quartz" records. Not drawn to scale.

Figure 5. A): The results of ray tracing in the velocity model of Figure 4A. A) travel time curves of the major phases. B): maximum penetration depths of refracted waves. C): travel times below the level of 195 km. Note that the far-offset refracted phases travel within the LVZ for about 60-70% of their total propagation times below this depth D): a sketch of the major seismic phases, reserved in Quartz records (Figure 2): P_n, P, P_{410}, P_{660}, primary refractions; WG_1, WG_2 - whispering-gallery modes; WG_{fs} - free-surface whispering-gallery mode; $P_{195}P$,$P_{410}P$ - reflections; P_{90M} - a multiple between 90 km and Moho. Gray circles indicate the triplication points of WG modes.

Figure 6. The same travel-time points as in Figure 5 overlain over the high-pass filtered record shown in (Figure 4A). The whispering-gallery modes correspond to the onset of the high-frequency teleseismic P_n. A triplication of the whispering-gallery mode is observed, but the fast branch can be followed to farther distances than in the modeled travel-time curves (indicated by arrow). Travel-time curves of the reflection from the 410-km discontinuity and of the multiple between the Moho and 90-km depth are also shown.

Figure 7. Ratios of the averaged power spectra within 0.5-2 Hz and 4-6 Hz in the offset range 2200-3000 km: a) first break window; b) teleseismic P_n window; c) high-frequency "post-shot noise", estimated at a signal level 100 sec after the onset of the teleseismic P_n. Note that the high-frequency teleseismic Pn exceeds the corresponding level in the first arrivals by about 8-12 dB, but is above the post-shot noise by only 10-15 dB.

Figure 8. Constraint on the attenuation contrast at the top of the LVZ obtained from the ratios of power spectra of deep refractions and of the teleseismic P_n using Equation (2). The quality factors Q_s (above the 195 km level) and Q_d (below this level) must correspond to a point below the graph. Dotted line represents the relation $Q_d=Q_s$, highlighting the contrast between Q_d and Q_s increasing with Q_s.

Figure 9. Travel-time plots obtained using ray tracing in 1-D velocity model with random scatterers located within two depth ranges. Top: first-order scattering within the depth range 0-140 km; bottom: : 1 first-order scattering within the depth range 140-195 km. Free-surface and Moho multiples are included in all cases. The rays are not allowed to penetrate into the LVZ (deeper then 195 km). Black dots represent the scattering of direct refracted waves and of WG mode, gray dots show the scattering of the free-surface WG mode and Moho multiples.

Figure 10. Inline component receiver gather from a) PNE 123; b) PNE 213; c) PNE 323. Instantaneous amplitude representation highlights the weaker events in the secondary arrivals in this large-scale plot. Travel times of the onsets of P-, S- and L_g phases are indicated. Note that L_g from PNE 123 increases its velocity in the region of Baltic shield, and its amplitude to the north is the highest of the three PNE's of the profile. To the SW from PNE 123, L_g is probably blocked by the

eastern flank of the Urals. Unfortunately, record lengths are shorter in this region. Teleseismic S wave from PNE 323 is the strongest of all three Quartz PNEs. Note that L_g amplitude from PNE 323 decays faster than S and probably faster than from the other two PNEs.

Figure 11. Travel times of the onsets of P- S- and L_g phases picked from PNE receiver gathers. PNE locations are indicated with black diamonds. Phases are labeled by their types and shot numbers. Top: P- and S- wave travel time curves (reduction velocity 8 km/sec); Bottom: S and L_g wave travel times (reduction velocity 4.5 km/sec). Note the shorter ranges within which L_g could be picked.

Figure 12. Vector amplitudes of picked P- S- and L_g phases versus offset for all three PNEs: a) PNE 123; b) PNE 213; c) PNE 323. Note that the scatter of the values of vector amplitude is lower than for scalar amplitude (Figure 13).

Figure 12b.

Figure 12c.

Figure 13. RMS amplitudes of all 3 components of the first break arrivals from PNE 323. P- wave amplitudes exhibit clear variations with the offset due to the arrivals of reflected phases and triplication points. S and L_g amplitude values are more scattered.

Figure 14. L_g/P amplitude ratios for the events picked in the records from PNE 323 between 400 and 1000 km (Figure 10c). These ratios show a fast attenuation of L_g amplitude with offset. Note that the stability of the ratio in the case of L_g/P is poorer than for L_g/S.

Figure 14.

Figure 15. Crustal and upper mantle structure along the "Quartz" profile from the Baltic shield to the Altai Mountains. Note a high-velocity root under the Ural Mountains.

Figure 16. Crustal structure from the Kola Peninsula to the Barents Sea basin, based on marine land recording.

Chapter 2

L_g Propogation and Crustal and Upper Mantle Structure

Elena Morozova, Igor Morozov and Scott Smithson

L_g phases in "Quartz" records

Examination of the PNE records (Figure 10) shows that S_n and L_g phases are generally very diffuse and hard to pick, and have long 20-40 s codas. Travel-time curves (Figure 11) show that L_g generally extinguishes at distances around 1000 km. The phases exhibit certain variability, especially among the horizontal components. However, instantaneous amplitude plots, low-pass filtered below 1 Hz (Figures 12-14) enable easy observation of many important features of these phases. These features can be summarized as follows:

- Travel time picks result in L_g propagation velocities ranging from 3.5 km/sec in the sedimentary basins to 3.75 km/s in the Baltic Shield.
- L_g generated by a PNE is weaker than S_n in all 3 shot gathers. With an exception of the northernmost part of the gather 12 3, where L_g propagates across the Baltic Shield.
- The above observation is especially true for shot 323, detonated in the crystalline rocks of Altai. In shot gather 323, strong S_n can be observed at distances near 3000 km, whereas L_g can be traced only to 1300 km. The latter is, however, the largest recorded distance of L_g propagation, but clearly its amplitude at 1100 km offset is still lower than L_g amplitude at the Baltic Shield from shot 123 at the same offset. We attribute these differences to higher energy and frequency of shot 323 and, on the other hand, to the seismic attenuation in the West Siberian Basin.
- Due to scatter of P_n amplitudes, the S_n-L_g ratio is more stable than the P_n-L_g amplitude, but scatter is lower for vector than for scalar amplitudes.
- Although some records of shot 123 corresponding to the Ural region have been truncated within the L_g coda (Figures 10 and 11), closer examination of these records and comparison to the records from shot 213 from the eastern side of the Urals, and also the absence of L_g at offsets exceeding 1000 km indicate that L_g is probably more strongly attenuated in the Pre-Ural depression.

Crustal and Upper Mantle Structure applying a travel-time tomographic inversion, we derived a model for the crust and uppermost mantle from the Baltic Shield to the West Siberian Basin (Schueller et al., in press). The main features are a high-velocity lower crust in the Kola Peninsula and a root under the Ural Mountains. A ray tracing model has been prepared for the crust and upper mantle down to a depth of 200 km (Figure 15). The main features of the crust are complicated structure under the Timan-Pechora Basin and a deep, about-50-km, high-velocity root under the Ural Mountains. The crustal thickness is around 40 km for most of the profile. An upper mantle boundary dip from 60 km to 90 km from NW to SE. A thin, low-velocity zone is indicated at about 140 km.

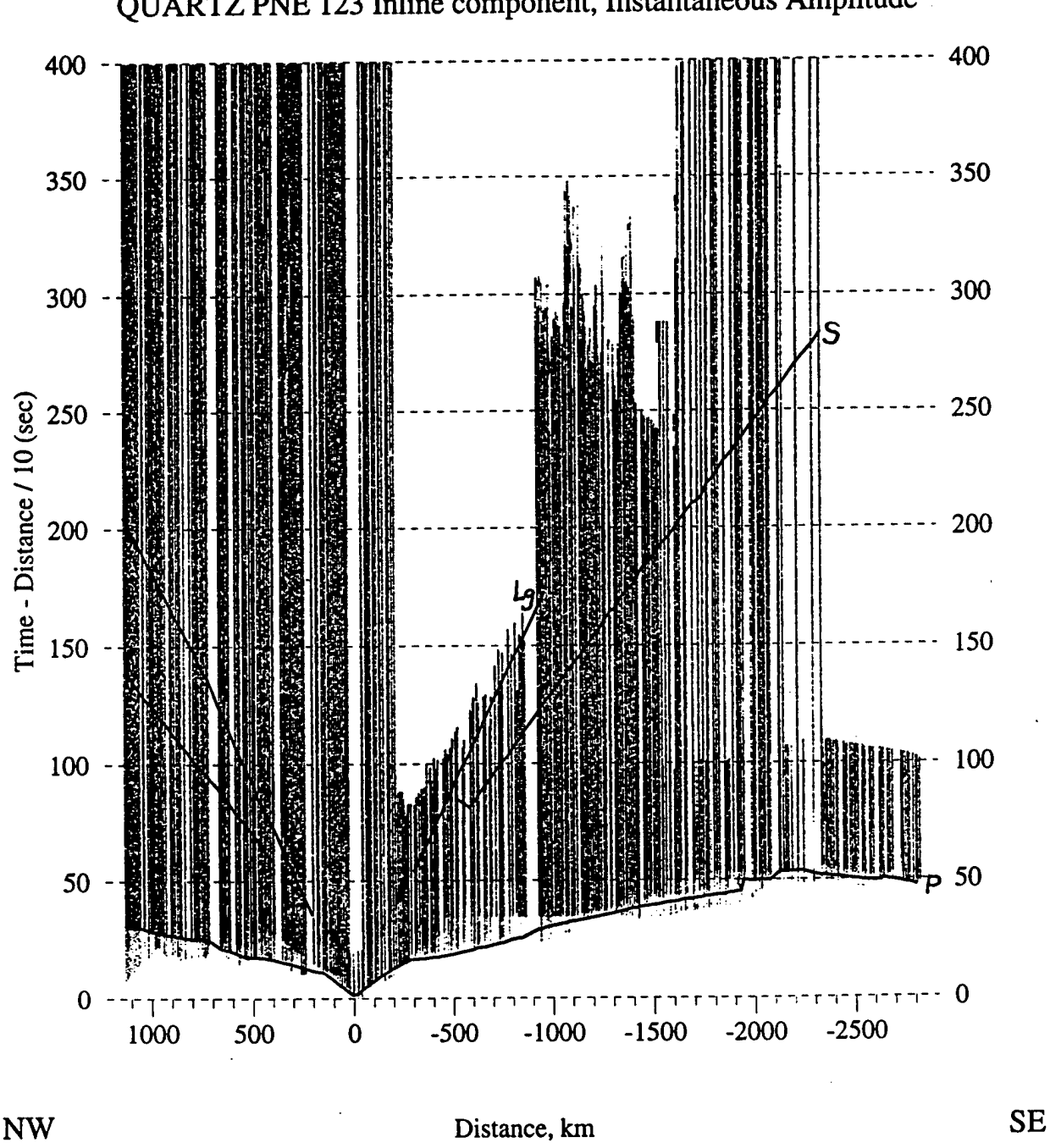

Figure 10. Inline component receiver gather from a) PNE 123; b) PNE 213; c) PNE 323. Instantaneous amplitude representation highlights the weaker events in the secondary arrivals in this large-scale plot. Travel times of the onsets of P-, S- and L_g phases are indicated. Note that L_g from PNE 123 increases its velocity in the region of Baltic shield, and its amplitude to the north is the highest of the three PNE's of the profile. To the SW from PNE 123, L_g is probably blocked by the eastern flank of the Urals. Unfortunately, record lengths are shorter in this region. Teleseismic S wave from PNE 323 is the strongest of all three Quartz PNEs. Note that L_g amplitude from PNE 323 decays faster than S and probably faster than from the other two PNEs.

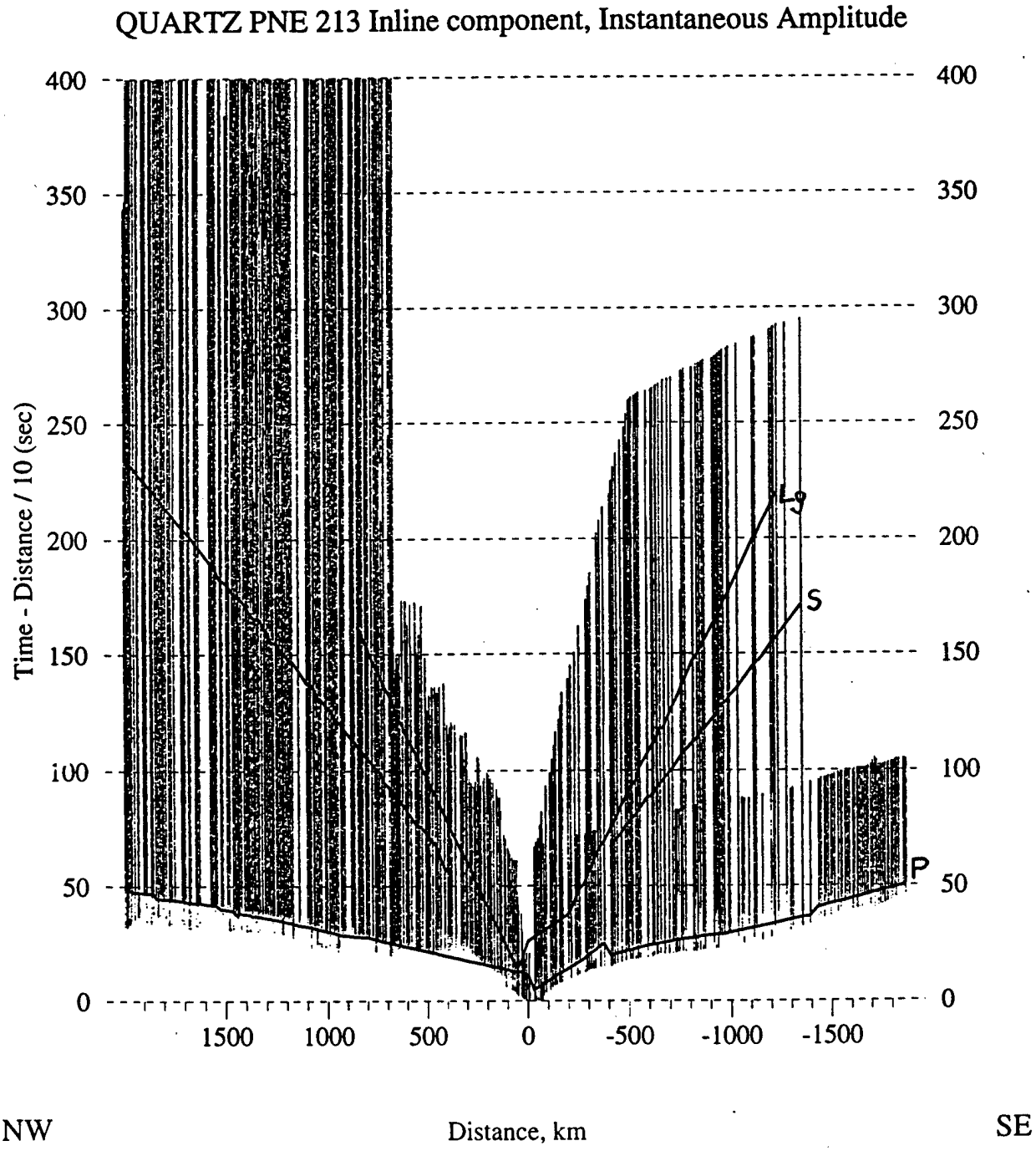
QUARTZ PNE 213 Inline component, Instantaneous Amplitude
Time - Distance / 10 (sec)
400
350
300
250
200
150
100
50
0
Lg
S
P
1500
1000
500
0
-500
-1000
-1500
NW
Distance, km
SE

Figure 10.

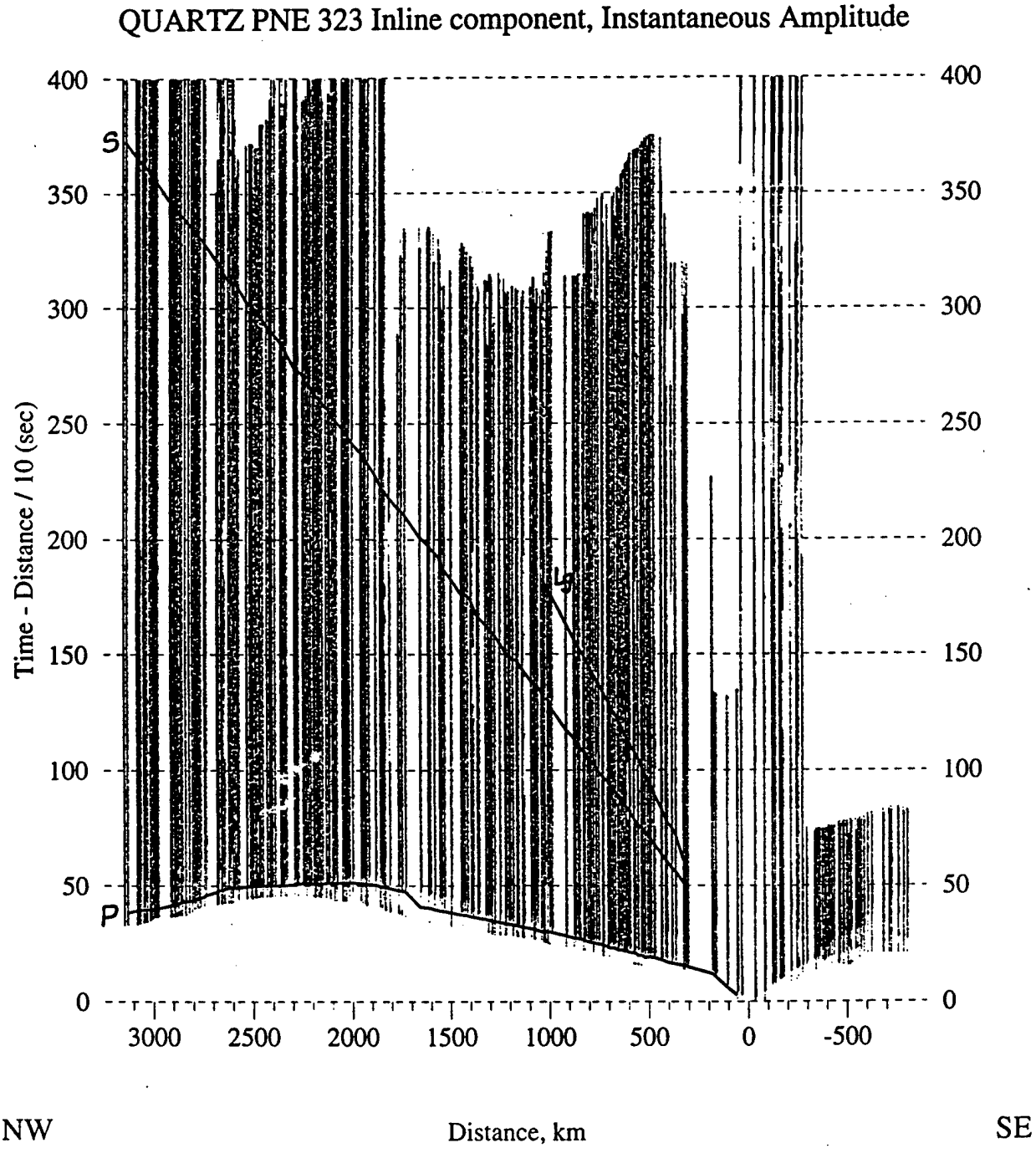
QUARTZ PNE 323 Inline component, Instantaneous Amplitude
Time - Distance / 10 (sec)
400
350
300
250
200
150
100
50
0
S
Lg
P
3000
2500
2000
1500
1000
500
0
-500
NW
Distance, km
SE

Figure 10.

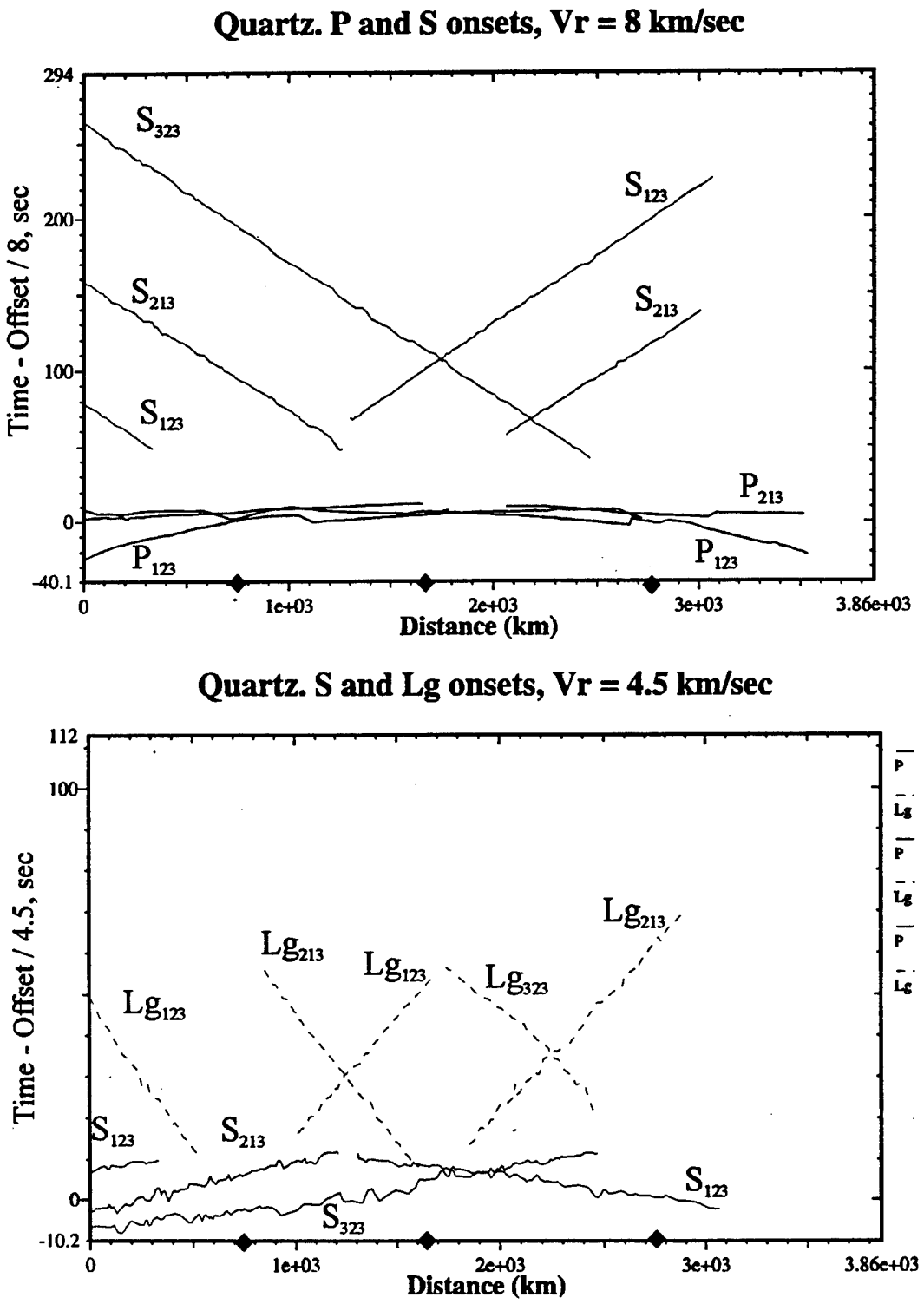

Figure 11. Travel times of the onsets of P- S- and L_g phases picked from PNE receiver gathers. PNE locations are indicated with black diamonds. Phases are labeled by their types and shot numbers. Top: P- and S- wave travel time curves (reduction velocity 8 km/sec); Bottom: S and L_g wave travel times (reduction velocity 4.5 km/sec). Note the shorter ranges within which L_g could be picked.

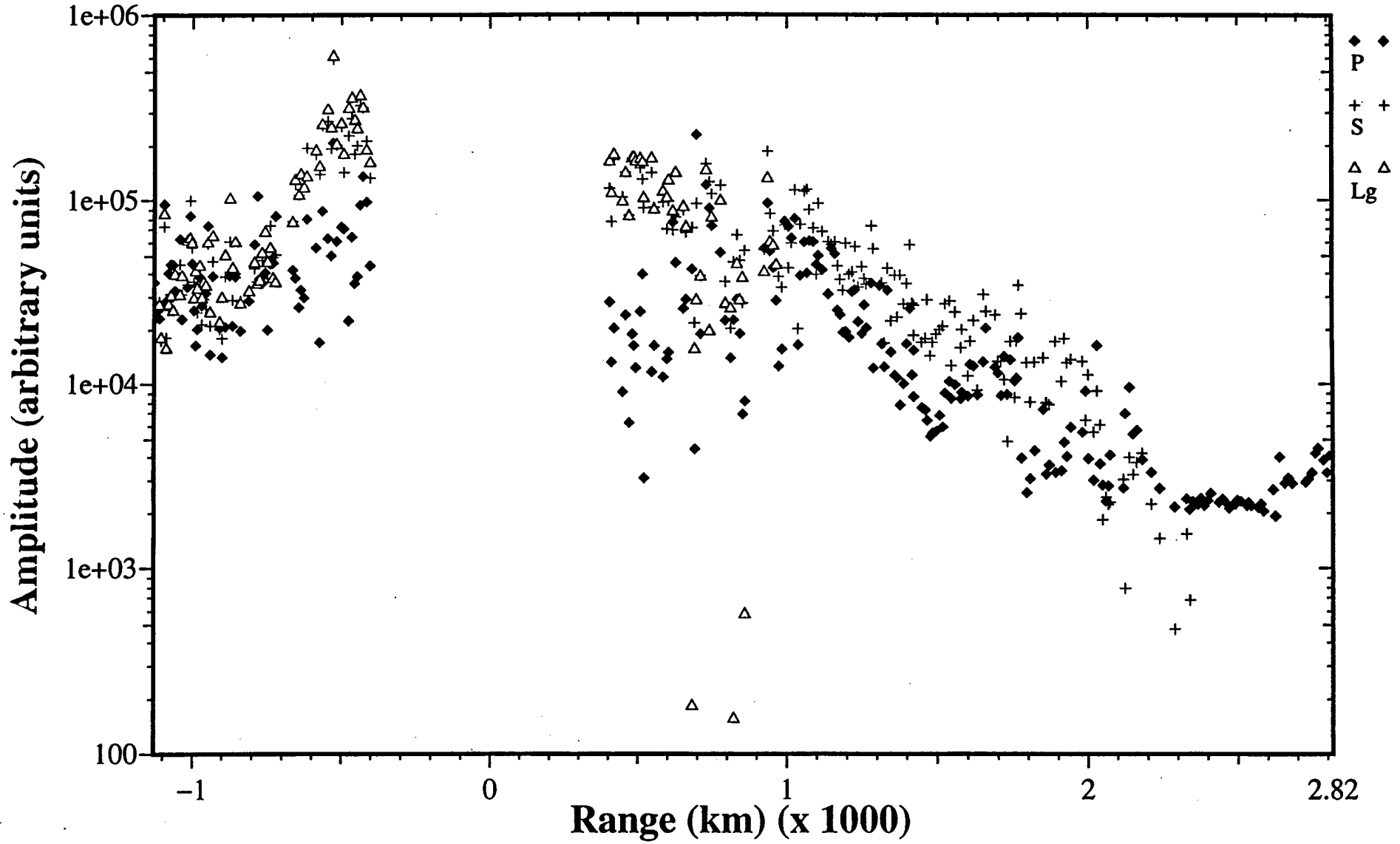

Figure 12. Vector amplitudes of picked P- S- and L_g phases versus offset for all three PNEs: a) PNE 123; b) PNE 213; c) PNE 323. Note that the scatter of the values of vector amplitude is lower than for scalar amplitude (Figure 13).

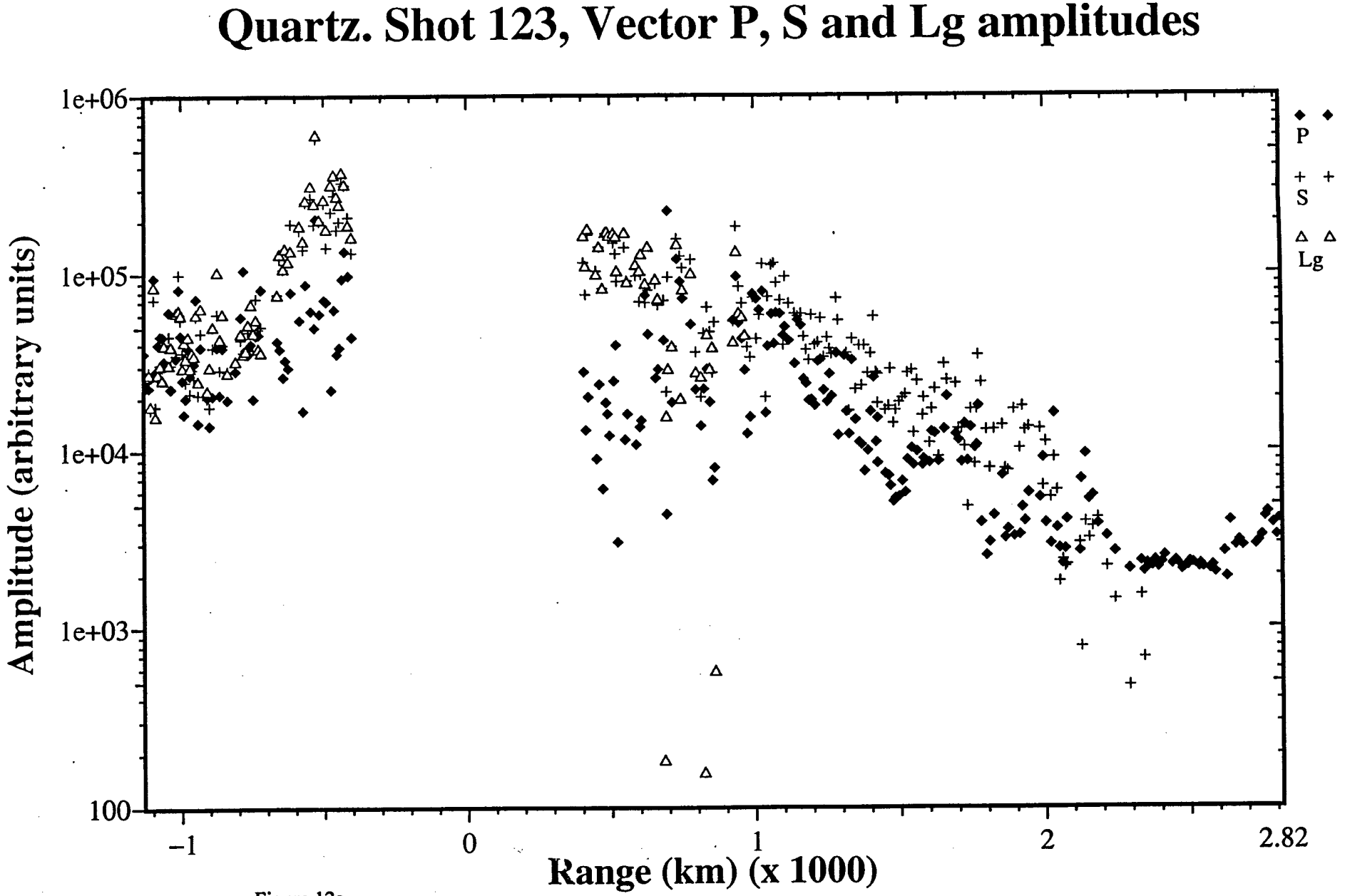
Quartz. Shot 123, Vector P, S and Lg amplitudes
Amplitude (arbitrary units)
1e+06
1e+05
1e+04
1e+03
100
−1
0
1
2
2.82
Range (km) (x 1000)
P
S
Lg

Figure 12a.

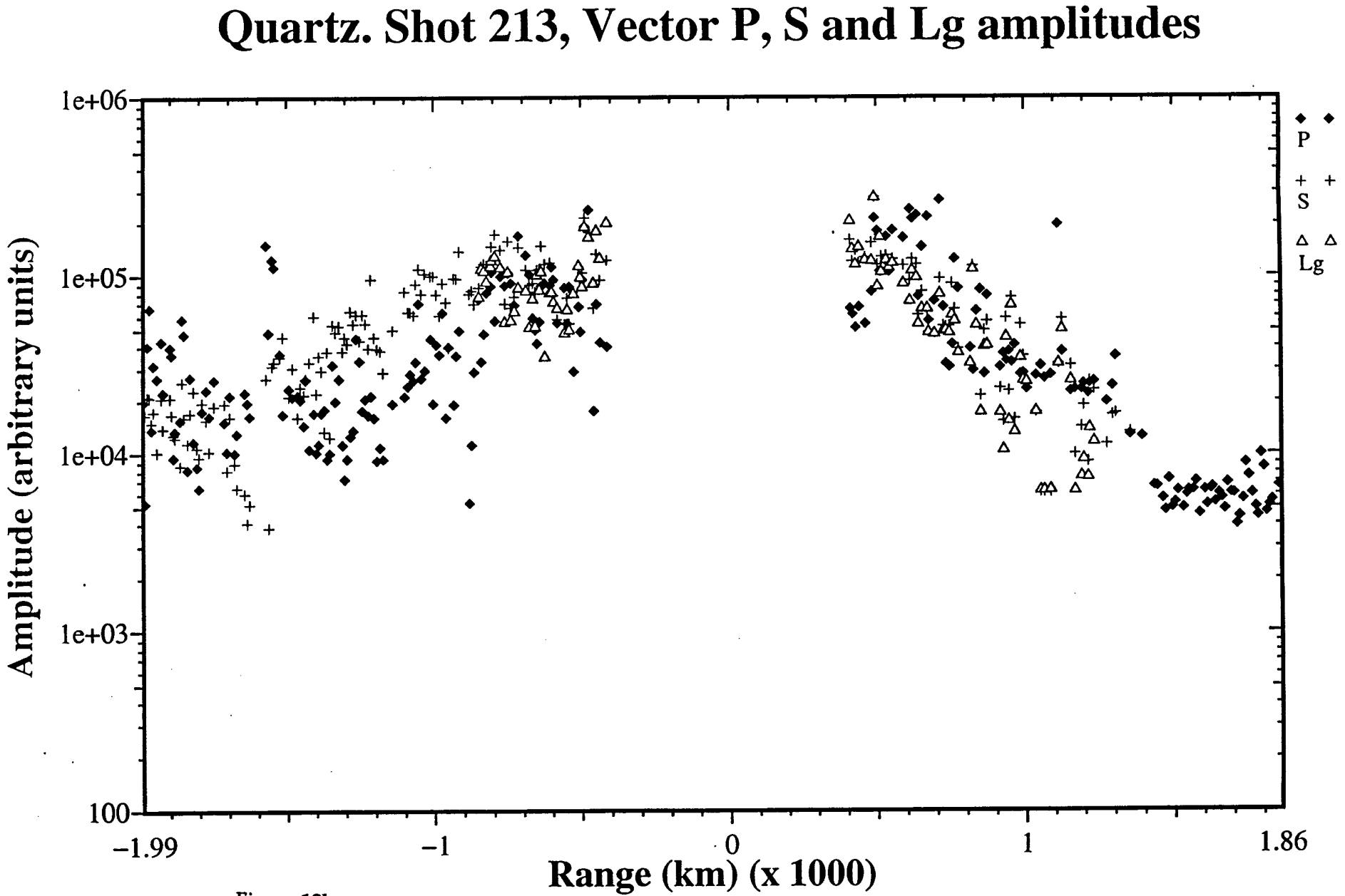
Quartz. Shot 213, Vector P, S and Lg amplitudes
Amplitude (arbitrary units)
1e+06
1e+05
1e+04
1e+03
100
−1.99
−1
0
1
1.86
Range (km) (x 1000)
P
S
Lg

Figure 12b.

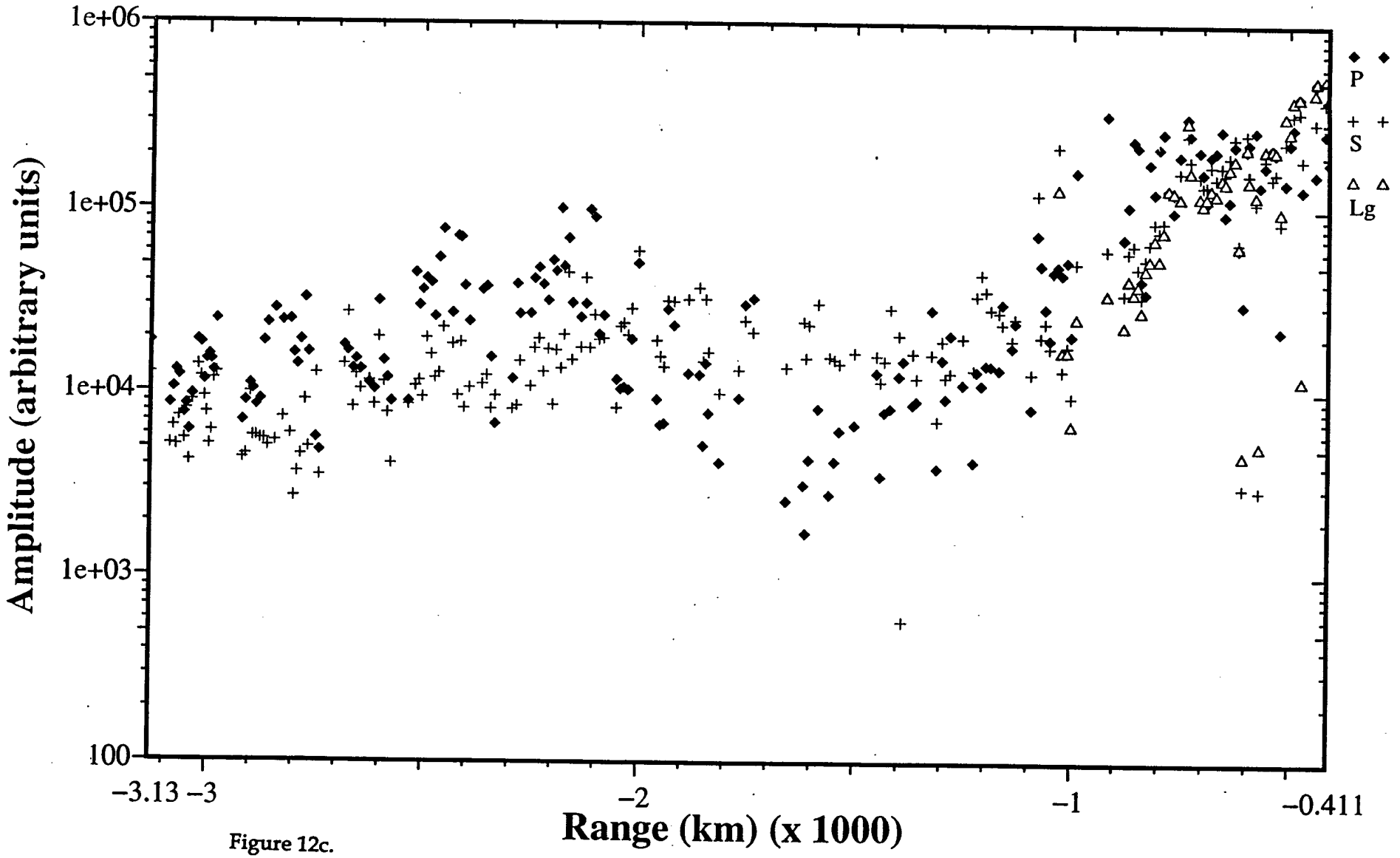
Quartz. Shot 323, Vector P, S and Lg amplitudes
1e+06
1e+05
1e+04
1e+03
100
Amplitude (arbitrary units)
−3.13
−3
−2
−1
−0.411
Range (km) (x 1000)
P
S
Lg

Figure 12c.

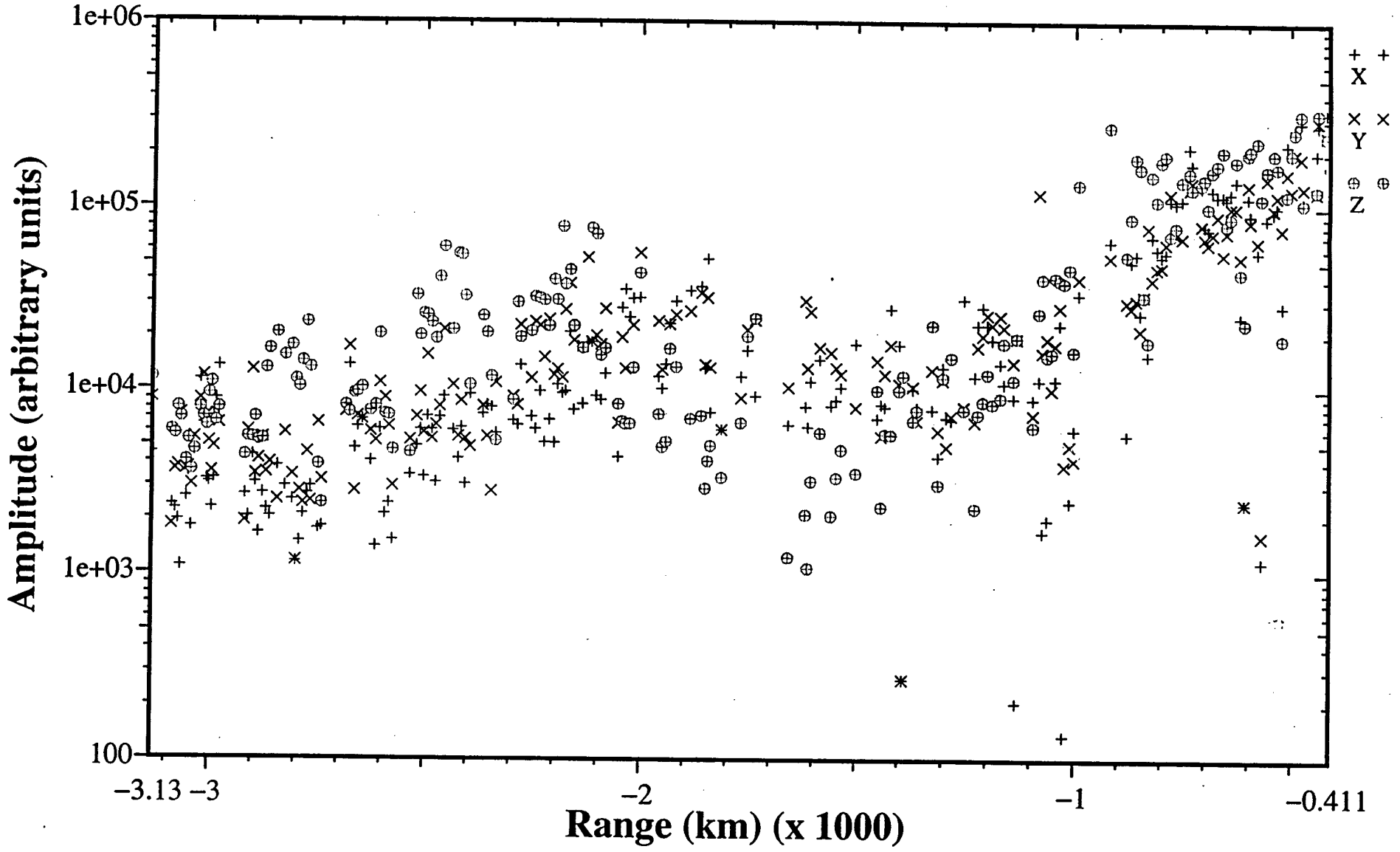

Figure 13. RMS amplitudes of all 3 components of the first break arrivals from PNE 323. P-wave amplitudes exhibit clear variations with the offset due to the arrivals of reflected phases and triplication points. S and L_g amplitude values are more scattered.

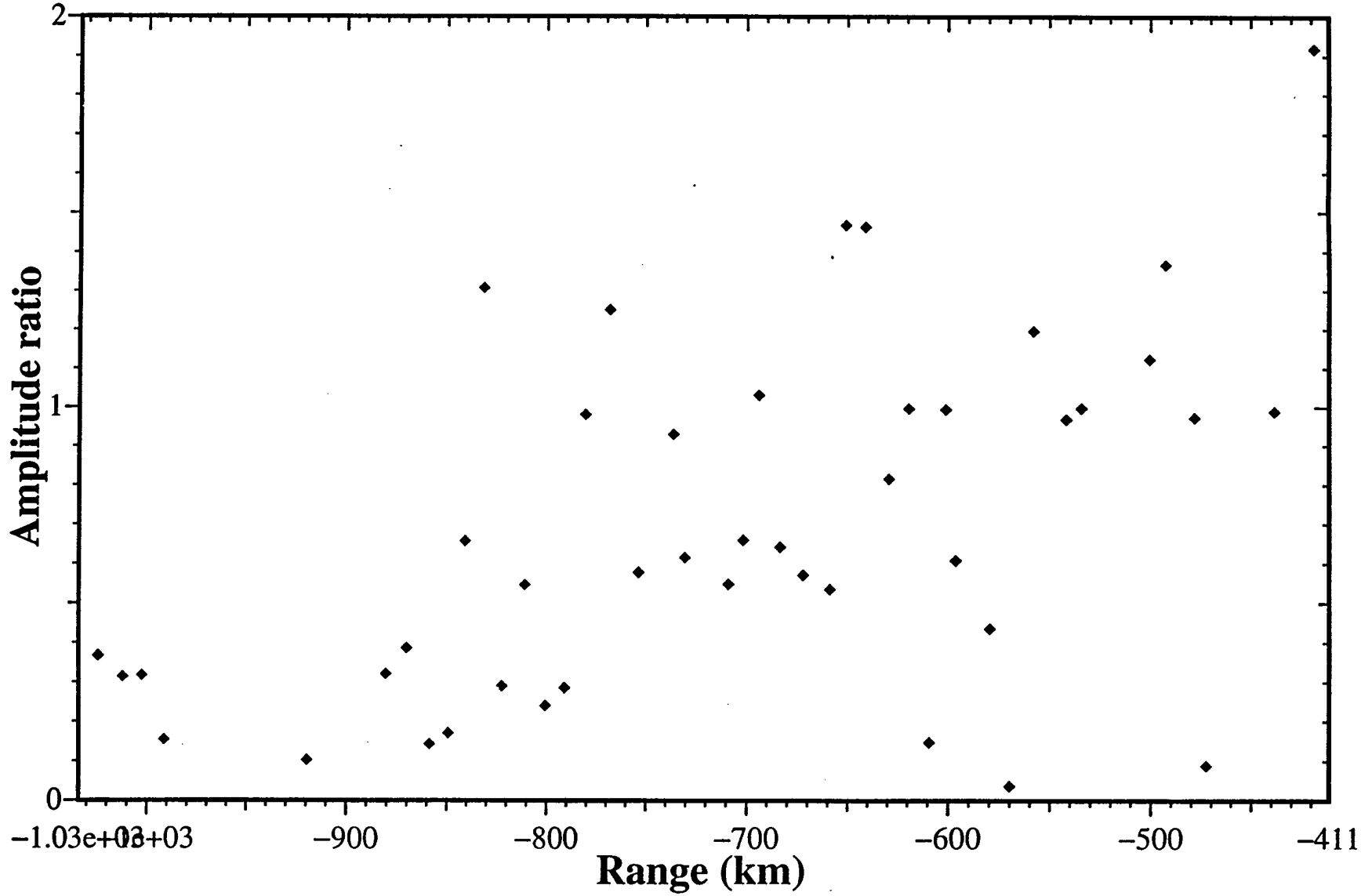

Figure 14. L_g/P amplitude ratios for the events picked in the records from PNE 323 between 400 and 1000 km (Figure 10c). These ratios show a fast attenuation of L_g amplitude with offset. Note that the stability of the ratio in the case of L_g/P is poorer than for L_g/S.

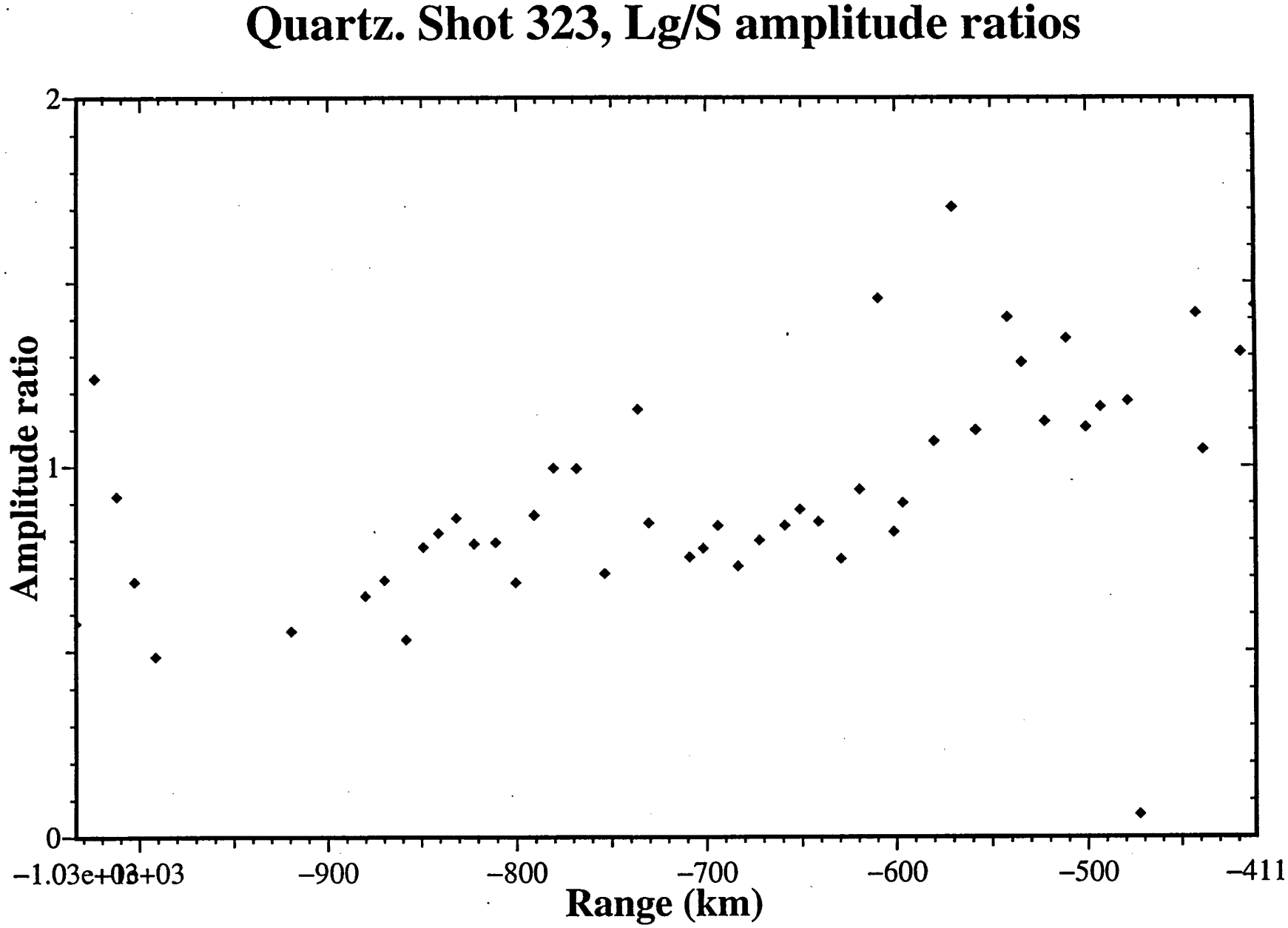
Quartz. Shot 323, Lg/S amplitude ratios
Amplitude ratio
2
1
0
−1.03e+03
−900
−800
−700
−600
−500
−411
Range (km)

Figure 14.

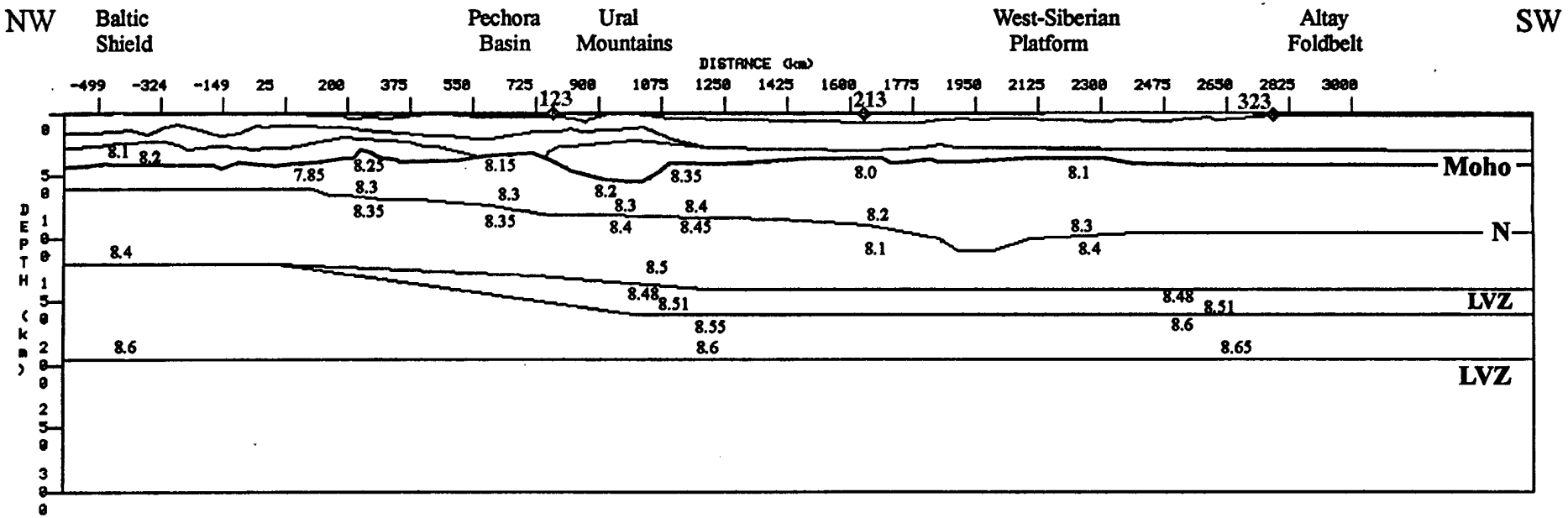

Figure 15. Crustal and upper mantle structure along the "Quartz" profile from the Baltic shield to the Altai Mountains. Note a high-velocity root under the Ural Mountains.

1995 wide-angle experiment in the Baltic Shield - Barents Sea Platform transition zone

As a part of research efforts directed at the analysis of L_g blockage in the Barents Sea area, AFOSR supported the participation of the University of Wyoming in a wide-angle offshore-onshore experiment on the north-eastern shelf of the Barents Sea, along the international geotraverse EU-3. The pilot investigations along parts of a 200 km sea and 100 km land profile at Kola Liinahamary-Barents Sea were carried out in August 1995. Seismic signals from marine 90-liter air gun sources were recorded at 5 surface sites using REFTEK seismographs. The moving marine source spacing had average values of 250 and 460 m.

The seismic velocity sections along the previously conducted geotraverse EU-3 (over the Baltic Shield - Barents Sea Platform transition zone) have a gap over an interval of about 100 km. The present project was aimed at covering this gap. Investigations along parts of 200 km. sea- and 700 km. surface-reference profile Lotta-Nikel-Kola-Liinahamary-Barents sea were carried out using a combination of seismic methods (marine and land CDP, DSS, refraction and PS earthquake converted wave methods with recording of air-gun signals, vibroseis signals, industrial blasts and earthquakes). Air-gun signals from marine sources were recorded in the Kola Superdeep- Borehole (8 km. depth) and at the drill site on the surface. 53 ocean bottom stations and 40 surface seismic recording stations ("Reftek's" and "Zemlja") were used for recording seismic signals from marine 90 liter air-guns. The waves produced by marine sources and reflected from the Moho discontinuity can be traced with large certainty for offset range 70 - 290 km. The thickness of the crust in the marine-land transition zone is 38-40 km. and slightly decreases towards the sea. The transition zone between the Baltic Shield, which is part of the East-European Platform, and the Barents Sea Plate is marked by seaward steps in the top of the basement. There is no common view among geologists as to which of these steps is the northern boundary of the Baltic Shield.

Joint field observations, in which 12 different organizations have taken part with different recording instruments make data processing a complex procedure. A seismic section along the Lotta - Kola - Barents Sea profile will allow us to clarify the velocity structure and the nature of seismic boundaries associated with the known geological information. It will be used for the creation of integrated East European Platform - Barents Sea Platform transition zone model.

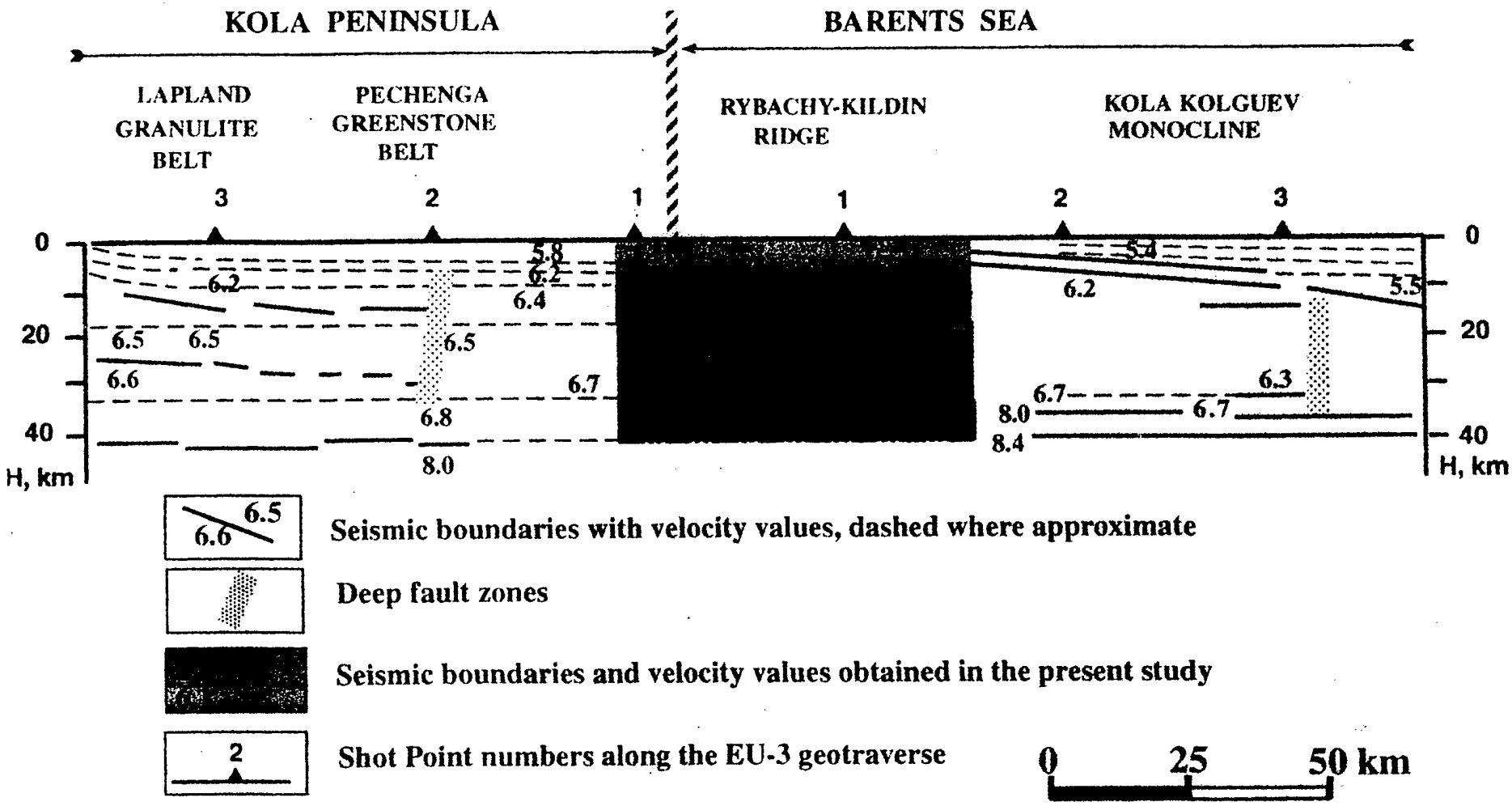

Figure 16. Crustal structure from the Kola Peninsula to the Barents Sea basin, based on marine land recording.

CHAPTER 3

James C. Schatzman

A SPECTRAL SCHEME FOR VISCOELASTIC SEISMIC MODELING

1. Objective

1.1. Introduction

Anelasticity and anisotropy of the earth play important roles in wave propagation, especially when waves travel long distances. Finite difference and finite element methods suffer from inaccuracies in the form of numerical dispersion and attenuation that make it difficult to simulate wave propagation over hundreds to thousands of wavelengths. The pseudospectral method exhibits very striking features of very low grid density and high efficiency, compared to the standard Cartesian discrete methods. The goal here is to simulate wave propagation in a region of about 2,000 km in azimuth and 100-200 km in depth; source frequencies are 0.5-10 Hz. Since wavelengths range from 120-4,000 meters, this represents propagation of about 500-20,000 wavelengths. Most FD or FE schemes either exhibit excessive numerical artifacts or are very inefficient for such problems.

Due to space limitations, we describe only the isotropic 2-D formulation. However, the anisotropic 3-D case is a straightforward extension and a detailed analysis is available from the authors.

1.2. 2-D Viscoelastic Wave Equations

When we talk about viscoelasticity, there are mainly two different ways to describe the strain–stress relationship, i.e. Voigt's model or Maxwell's model, each corresponding to connections of the elastic and viscous behavior in parallel and series. For computational consideration, Voigt's model is highly recommended because of its simplicity and generality.

For an isotropic-elastic medium the stress-strain relation is

$$\sigma_{ii} = \overline{\lambda}\Delta + 2\overline{\mu}\varepsilon_{ii}, \qquad i = 1,2,3, \tag{1}$$

$$\sigma_{ij} = \overline{\mu}\varepsilon_{ij}, \qquad i \neq j, \;\; i,j = 1,2,3, \tag{2}$$

where $\overline{\lambda} = \lambda + \lambda' \frac{\partial}{\partial t}$ and $\overline{\mu} = \mu + \mu' \frac{\partial}{\partial t}$. It is beyond the scope of this paper to include a derivation, but we find that λ' and μ' are related to the Q for P- and S-wave propagation by

$$Q_p = \frac{\sqrt{(\lambda + 2\mu)^2 + k^2(\lambda' + 2\mu')^2 v_p^2} + \lambda + 2\mu}{2(\lambda' + 2\mu')kv_p}. \tag{3}$$

$$Q_s = \frac{\sqrt{\mu^2 + k^2\mu'^2 v_s^2} + \mu}{2\mu' k v_s}. \tag{4}$$

We see that in this model, Q_p and Q_s are not constant but are functions of wavenumber. The viscoelastic equations of motion are

$$\rho\frac{\partial^2 u_i}{\partial t^2} = \frac{\partial}{\partial x_i}[(\overline{\lambda} + \overline{\mu})\theta] + \nabla \cdot (\overline{\mu}\nabla u_i) + f_i, \;\; i = 1,2,3, \tag{5}$$

where $\mathbf{f} = (f_1, f_2, f_3)^T$ is the applied force.

If in a region the medium is partially homogeneous (μ and μ' are constants), then in this region we have

$$\rho\frac{\partial^2 \theta}{\partial t^2} = (\overline{\lambda} + 2\overline{\mu})\Delta\theta, \tag{6}$$

and

$$\rho\frac{\partial^2 \omega}{\partial t^2} = \overline{\mu}\Delta\omega. \tag{7}$$

where $\theta = \nabla \cdot \mathbf{u}$ and $\omega = \nabla \times \mathbf{u}$. Thus we see that even in viscoelastic media the dilation wave equation is similar to a "pure" P-wave equation and the rotational wave equations coincides in form with the "pure" S-wave equation.

1.4. About the Grids

The strategy adopted for choosing the mapping function η is to flatten the surface and major contours. "Major contours" are those interfaces, typically the basement and moho, that are continuous across the section. Fig.17 shows one of a set of "deep sedimentary basin" models that are being tested. Fig.18 shows a model, derived from seismic data, for a trans-Urals DSS path.

Once the "major contours" are identified, the average travel time between the contours is computed (p-waves have been used so far), and constant values of η are assigned to the major contours so that the differences in η are proportional to the travel time. In this way, increments of constant $\Delta\eta$ correspond roughly to equal increments of travel time. This is done so as to improve the stability properties of the time integration.

1.5. Preliminary Results

Preliminary calculations indicate that it is practical to simulate wave propagation for 2-D models of about 2,000 by 200 km. Such simulations require several days of compuation on a SGI Power Challenge (300 MFlops).

We are in the process of quantifying the effects of particular types of crustal features on regional waveforms. Features under study include deep sedimentary basins (see Fig.17), moho uplift and lateral variation in surface features. Also, some realistic models (such as the Soviet DSS model in Fig.18) are currently being tested.

2. Recommendations and Future Plans

Other authors have performed simulations for particular models (e.g., Jih (1994) uses a finite difference method); there is not yet completed a comprehensive and quantitative study of the effects of crustal features. Our plan is to use a series of models, for example the deep sedimentary basin models, varying the size and elastic parameters of the basin, to determine how the effects of such basins on crustal wave propagation, such as attenuation of L_g, depend on the parameters of the basin. Additionally, we will study the effects of moho uplift, combined basin and uplift, and surface topographical roughness and other surface features.

One weakness of this method is that, because of its 2-D nature, amplitudes and decay times are not correct, and relative amplitudes of differing phases are not readily obtainable. Although the method described in this paper can readily be applied to the 3-D problem, it is apparent that elastic wavefield computations in a region of 2,000 by 2,000 by 200 km are not practical with any computer available to the authors. However, two acceleration techniques may be employed when solving the problem of wave propagation between two points (source and receiver):

1. Model only a narrow channel between the source and receiver (see Fig.19). Use absorbing boundary conditions on the lateral boundaries to avoid reflections or wrap-around.
2. Use smaller tracking grids that follows the major wave fronts. A full simulation would then require several runs, each to capture the modes with essentially different paths, but each run would be much quicker than a global computation.

1. Bayliss, A., Jordan, K. E., Lemesurier, B. J. and Turkel, E., 1986, A fourth-order accurate finite-difference scheme for the computation of elastic waves: *Bulletin of the Seismological Society of America*, 76, pp. 1115–1132.
2. Carcione, J. M., 1992, Modeling anelastic singular surface waves in the earth: *Geophysics*, 57, pp. 781–792.
3. Carcione, J. M., Kosloff, D. and Kosloff, R., 1988, Wave propagation simulation in an elastic anisotropic (transversely isotropic) solid: *Q. J. Mech. Appl. Math.*, 41, pp. 319–415.
4. Carcione, J. M., Kosloff, D., Behle, A. and Serian, G., 1992, A spectral scheme for wave propagation simulation in 3-D elastic-anisotropic media: *Geophysics*, 57, pp. 1593–1607.
5. Fornberg, B., 1988, The pseudospectural method: Accurate representation of interfaces in elastic wave calculations: *Geophysics*, 53, pp. 625–637.
6. Fornberg, B., 1987, The pseudospectrul method: Comparisons with finite difference for the elastic wave equation: *Geophysics*, 52, pp. 483–501.
7. Fornberg, B. and Sloan, D. M., 1994, A review of pseudospectral methods for solving partial differential equations: *Acta Numerica*, pp. 203–267.
8. Gottlieb, D., Gunzburger, M. and Turkel, E., 1982, On numerical boundary treatment of hyperbolic systems for finite difference and finite element methods: *SIAM Journal of Numerical Analysis*, 19, pp. 671–682.
9. R.-D. Jih, 1994, Numerical Modeling of Crustal Phase Propagation in Irregular Waveguides, 16th PL/AFOSR Seismic Symposium, pp. 173-81. PL-TR-94-2217, ADA284667

10. Nielsen, P., Flemming, I, Berg, P. and Skovgaard O., 1994, Using the pseudospectrual technique on curved grids for 2D acoustic forward modeling: *Geophysical Prospecting*, 42, pp. 321–341.
11. Kosloff, D., Kessler, D., Filho, A. Q., Tessmer, E., Behle, A. and Strahilevitz, R., 1990, Solution of the equations of dynamic elasticity by a Chebychev spectral method: *Geophysics*, 55, pp.734–748.
12. Kindelan, M., Kamel, A. and Sguazzero, P., 1990, On the construction and efficiency of staggered numerical differentiators for the wave equation: *Geophysics*, 55, pp. 107–110.
13. Sheriff, R. E., and Geldart, L. P., 1982, *Exploration Seismology*, Vol. 1:*History, Theory and Data Acquisition*, Cambridge, Cambridge University Press.
14 Sheriff, R. E. and Geldart, L. P., 1983, *Exploration Seismology*, Vol. 2: *Data-processing and Interpretation*, Cambridge, Cambridge University Press.
15. Tessmer, E. and Kosloff, D., 1994, 3-D elastic modeling with surface topography by a Chebyshev spectral method: *Geophysics*, 59, pp. 464–473.
16. Tessmer, E., Kosloff, D. and Behle, A., 1992, Elastic wave propagation simulation in the presence of surface topography: *Geophysical Journal International*, 108, pp. 620–632.
17. Meng, Z., Feng, Y. and Fan, Z., 1992, Radiation boundary conditions for complicated wave propagations: *Chinese Journal of Geophysics*, 34, pp.509–516.
18. Fan, Z. and Teng, Y., 1988, Numerical simulations of viscoelastic waves: *Acta Geophysica Sinica*, 31, pp. 198–209.

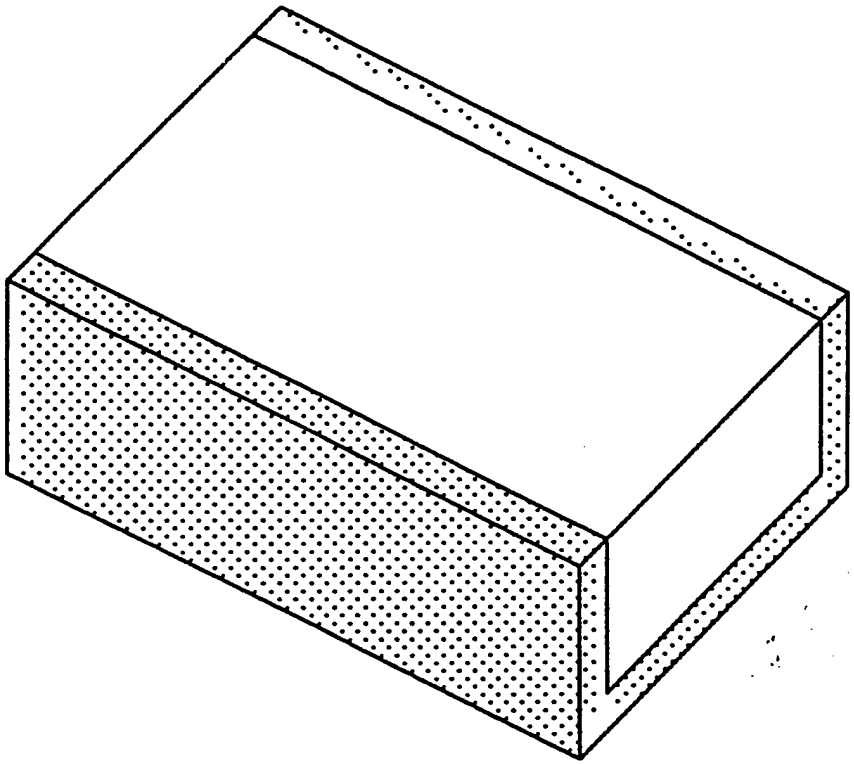

Active Computational Region

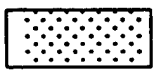

Attenuating Layer

Figure19. Sketch of three-dimensional computational domain showing attenuating layers at bottom and sides.